

Supplementary Material (ESI) for *CrystEngComm*

Four dual-functional Luminescent Zn(II)-MOFs based on 1,2,4,5-  
benzenetetracarboxylic acid with pyridylbenzimidazole ligands for detection  
of Iron (III) ions and acetylacetone

Yong-Sheng Shi<sup>a</sup>, Qiang Yu<sup>a\*</sup>, Jian-Wei Zhang<sup>b</sup>, Guang-Hua Cui<sup>a\*</sup>

<sup>a</sup>*College of Chemical Engineering, Hebei Key Laboratory for Environment Photocatalytic and  
Electrocatalytic Materials, North China University of Science and Technology, No. 21 Bohai*

*Road, Caofeidian new-city, Tangshan, Hebei, 063210, P. R. China*

<sup>b</sup>*Tangshan Normal University, Tangshan, Hebei, 063210, P. R. China*

\*Corresponding author: Guang-Hua Cui; Qiang Yu

Fax: +86-0315-8805462. Tel: +86-0315-8805460

E-mail: [tscghua@126.com](mailto:tscghua@126.com).

E-mail: [yuqiang@ncst.edu.com](mailto:yuqiang@ncst.edu.com)

## CONTENTS

Section 1. Experimental Section

Section 2. Supplementary Tables and Structural Figures

Section 3. Supplementary Characterizations

## **Section 1. Experimental Section**

1. Sensing experiments
2. The process of the pH-dependent PXRD and fluorescence experiment of inorganic anions and solvents for MOFs **1–4**
3. Electrochemical measurement
4. DFT calculation

## 1. Sensing experiments

50 mg MOFs **1–4** after finely grinding was dispersed into 50 mL EtOH to generate the suspension solution by an ultrasound method (conditions: 25 °C, 210 W and 30 min). 0.30 µL of different organic solvents were slowly dropped into 4.00 mL EtOH/MOFs **1–4** and ultrasonically treated under same conditions. The solvents used in the tests were ethanol (EtOH), acetonitrile (MeCN), *N*-butanol (NBA), dimethyl sulfoxide (DMSO), dichloromethane (DCM), cyclohexane (CYH), methanol (MeOH), acetone (AT), acetylacetonate (acac), ethylene glycol (EG) and *N*-methyl pyrrolidone (NMP), *N,N*-Dimethylformamide (DMF), *N,N*-Dimethylacetamide (DMA), Ethyl acetate (EAC). The other suspension of MOFs **1–4** in water (H<sub>2</sub>O/MOFs **1–4**) were obtained through the analogous approach to discuss the fluorescence of MOFs **1–4** for sensing acac in water media. For cation sensing, 4 mg powder and 4 mL (EtOH/H<sub>2</sub>O 1:1, v/v) of  $5 \times 10^{-4}$  M different M<sup>x+</sup>(NO<sub>3</sub>)<sub>x</sub> solutions were put into 5 mL glass vial (M<sup>x+</sup> = Na<sup>+</sup>, K<sup>+</sup>, Al<sup>3+</sup>, Ca<sup>2+</sup>, Cr<sup>3+</sup>, Fe<sup>3+</sup>, Co<sup>2+</sup>, Ni<sup>2+</sup>, Cu<sup>2+</sup>, Zn<sup>2+</sup>, Ag<sup>+</sup>, Cd<sup>2+</sup>, Ba<sup>2+</sup>, La<sup>3+</sup>, Sm<sup>3+</sup>, Hg<sup>2+</sup>, or Pb<sup>2+</sup>). Then, the mixtures were handled with ultrasonic wave to measure the fluorescence recognition. Finally, the fluorescence quenching efficiency (Q) and  $K_{sv}$  values are calculated by Eq. (1) and the Stern–Volmer Eq. (2) respectively.

$$Q = [(I_0 - I)/I_0] \times 100\% \quad (1)$$

$$I_0/I = 1 + K_{sv} [M] \quad (2)$$

Wherein  $I_0$  and  $I$  represent the fluorescence emission intensities of MOFs **1–4** without and with analyte respectively;  $K_{sv}$  is on behalf of the quenching constant;  $[M]$  is the concentration of analyte (mol L<sup>-1</sup>).

## 2. The process of the pH-dependent PXRD and fluorescence experiment of inorganic anions and solvents for MOFs **1–4**

The test criteria for the efficiency of sensors is whether fluorescent sensors exist safely in solutions with different pH values. Initially, 4 mg of MOFs **1–4** were dispersed in 4 mL of deionized water with a pH range of 1 to 14 (pH adjustment with 1 M HCl or 1 M NaOH) and stored for 24 h, then the samples were allowed to air dry and used for PXRD measurements.

By using 1 M HCl or NaOH, solutions containing Fe<sup>3+</sup>/acac have adjusted pH from 1.0 to 14.0, then 4 mg of MOFs **1–4** were dispersed into 4 mL above-mentioned solutions and sonicated for 30 minutes to obtain MOFs **1–4** suspensions with different pH. Subsequently, a quartz cuvette

was decanted with the solutions containing the suspended MOFs 1–4. Finally, an Edinburgh FS5 fluorescence spectrophotometer at room temperature obtained the emission spectra from 300 to 450 nm using an excitation wavelength of 300–330 nm.

### 3. Electrochemical measurement

A CHI660E electrochemical workstation (Chenhua, Shanghai, China) was employed to investigate the cyclic voltammogram (CV) of MOFs 1–4 in the 0.1 mol L<sup>-1</sup> Na<sub>2</sub>SO<sub>4</sub> aqueous solutions. A glassy carbon electrode (GCE, Ø = 3 mm) was coated with MOFs 1–4 as follows: 24 mg powder of MOFs 1–4 were ultrasonicated in 4 mL ethanol for 2 h. Then, 30 µL of the suspension was placed on the surface of the GCE and dried in air for 30 min at room temperature. After that, 10 µL of 0.2% Nafion solution was transferred quantitatively onto the surface of the modified GCE. Finally, the MOFs 1–4/GCE was obtained after drying in air for about 1 h. The modified MOFs 1–4/GCE, saturated calomel electrode (SCE), and platinum electrode were applied as the working electrode, reference electrode, and auxiliary electrode, respectively. The electrochemical behavior of MOFs 1–4 were evaluated by CV technique with the scan rate of 50 mV s<sup>-1</sup>.

### 4. DFT calculation

The acac molecule and Fe<sup>3+</sup> ions were optimized based on the previously reported method. HOMO–LUMO energies and the size of each molecule were obtained using Materials Studio 8.0 version.<sup>1</sup> In DFT calculation, the HOMO–LUMO energies are performed with the DMol3 package.<sup>2</sup> The generalized gradient approximation (GGA) with the Perdew–Burke–Ernzerhof (PBE) functional and double numerical plus polarization (DNP) basis set was used. The generalized gradient approximation (GGA) underestimates the HOMO–LUMO energies while the B3LYP overestimates the HOMO–LUMO energies. Therefore, the B3LYP functional was also used to evaluate the HOMO–LUMO energies.

### References

- (1) Dong, J. Q.; Tummanapelli, A. K.; Li, X.; Ying, S. M.; Hirao, H.; Zhao, D. Fluorescent porous organic frameworks containing molecular rotors for size-selective recognition. *Chem. Mater.*, **2016**, 28, 7889–7897.
- (2) Perdew, J. P.; Chevary, J. A.; Vosko, S. H.; Jackson, K. A.; Pederson, M. R.; Singh, D. J.; Fiolhais, C. *Phys. Rev. B: Condens. Matter.*, **1992**, 46, 6671–6687.
- (3) Li Y, Cao Y, Gao J, et al. Electrochemical properties of luminescent polymers and polymer light-emitting electrochemical cells. *Synthetic Metals*, 1999, 99(3): 243–248.



## **Section 2. Supplementary Tables, Structural Figures and Scheme**

Table Titles:

**Table S1.** Crystal and refinement data for MOFs 1–4

**Table S2.** Selected bond lengths [ $\text{\AA}$ ] and angles [ $^\circ$ ] for complexes MOFs 1–4

**Table S3** Thermal stability analysis for MOFs 1-4

**Table S4.** The BET surface area and porosity of MOFs 1–4

**Table S5.** HOMO-LUMO energies (in eV) for MOFs 1–4, L1–L4, H<sub>4</sub>BTEC and analytes

**Table S1** Crystal data and structure refinements for the MOF 1-4

MOF	1	2	3	4
Chemical formula	C <sub>37</sub> H <sub>36</sub> N <sub>6</sub> O <sub>7.5</sub> Zn	C <sub>20</sub> H <sub>18</sub> N <sub>3</sub> O <sub>5.5</sub> Zn	C <sub>41</sub> H <sub>36</sub> N <sub>6</sub> O <sub>10</sub> Zn <sub>2</sub>	C <sub>27</sub> H <sub>18</sub> N <sub>3</sub> O <sub>9</sub> Zn <sub>2</sub>
Formula weight	745.17	453.74	903.50	659.18
Crystal system	Triclinic	Triclinic	Triclinic	Triclinic
Space group	<i>P</i> $\bar{1}$	<i>P</i> $\bar{1}$	<i>P</i> $\bar{1}$	<i>P</i> $\bar{1}$
<i>a</i> (Å)	9.5737(5)	8.8439(10)	10.8405(3)	8.4780(2)
<i>b</i> (Å)	11.8435(5)	10.2104(2)	11.9854(4)	11.9324(3)
<i>c</i> (Å)	15.8044(9)	10.7211(2)	15.6874(9)	13.6431(3)
$\alpha$ (°)	75.085(4)	99.388(2)	68.832(3)	105.021(2)
$\beta$ (°)	75.490(4)	96.1840(10)	82.564(2)	101.269(2)
$\gamma$ (°)	84.345(4)	101.9350(10)	750177(2)	105.692(3)
<i>V</i> (Å <sup>3</sup> )	1675.28(16)	924.41(3)	1835.87(11)	1229.90(6)
<i>Z</i>	2	2	2	2
<i>D</i> <sub>calcd</sub> (g/cm <sup>3</sup> )	1.487	1.630	1.634	1.780
Absorption coefficient, mm <sup>-1</sup>	0.796	1.371	1.379	2.015
<i>F</i> (000)	780	446	928	666
Crystal size, mm	0.21 x 0.21 x 0.19	0.20 x 0.16 x 0.12	0.21 x 0.21 x 0.19	0.20 x 0.16 x 0.12
$\theta$ range, deg	3.562-61.286	4.154-61.088	4.690-61.152	4.062-61.134
Index range <i>h, k, l</i>	-13/13, -16/16, -14/22	-12/12, -14/14, -14/15	-15/15, -17/17, -22/21	-11/11, -17/16, -19/19
Reflections collected	42306	26764	53347	35757
Independent reflections ( <i>R</i> <sub>int</sub> )	9733(0.0620)	5385 (0.0305)	10741(0.0385)	7205 (0.0452)
Data/restraint/parameters	9733 / 0 / 434	5835 / 0 / 277	10741 / 0 / 536	7205 / 0 / 377
Goodness-of-fit on <i>F</i> <sup>2</sup>	1.087	1.078	1.021	1.077
Final <i>R</i> <sub>1</sub> , <i>wR</i> <sub>2</sub> ( <i>I</i> > 2σ( <i>I</i> ))	0.1071, 0.2672	0.0333, 0.0860	0.0410, 0.0833	0.0485, 0.1301
Largest diff. peak and hole	2.08, -2.31	0.33, -0.38	0.68, -0.77	1.91, -0.93

**Table S2** Selected Bond Lengths [ $\text{\AA}$ ] and Angles [ $^\circ$ ] for the MOFs **1-4**

Parameter	Value	Parameter	Value
<b>1</b>			
Zn1–O1	1.940(5)	Zn1–N1	2.073(5)
Zn1–O3A	1.959(5)	Zn1–N6B	2.064(5)
O1–Zn1–O3A	113.7(2)	O3A–Zn1–N1	103.2(2)
O1–Zn1–N1	112.6(2)	O3A–Zn1–N6B	132.4(2)
O1–Zn1–N6B	93.0(2)	N6B–Zn1–N1	101.4(2)
<b>2</b>			
Zn1–O1	1.937(14)	Zn1–N1	2.011(14)
Zn1–O3A	1.943(13)	Zn1–N6B	2.055(15)
O1–Zn1–O3A	107.60(6)	O1–Zn1–N1	123.43(6)
N1–Zn1–O3A	107.67(6)	O1–Zn1–N3B	97.60(6)
N3A–Zn1–O3A	112.20(6)	N1–Zn1–N3B	108.02(6)
<b>3</b>			
Zn1–O5	1.965(15)	Zn1–O9	1.995(17)
Zn1–O1	1.928(16)	Zn1–N1	1.989(18)
Zn2–O4A	1.991(15)	Zn2–O7	1.9293(14)
Zn2–N4B	2.086(17)	Zn2–N6C	2.067(19)
O5–Zn1–O9	98.79(7)	O7–Zn2–O4A	127.15(7)
O5–Zn1–N1	104.78(7)	O7–Zn2–N4B	100.76(7)
O1–Zn1–O5	105.08(8)	O7–Zn2–N6C	117.26(7)
O1–Zn1–O9	110.91(8)	O4A–Zn2–N4B	102.12(7)
O1–Zn1–N1	113.77(8)	O4A–Zn2–N6C	106.80(7)
N1–Zn1–O9	120.83(8)	N4b–Zn2–N6C	96.09(7)
<b>4</b>			
Zn1–O6C	2.025(2)	Zn1–O8C	2.107(3)
Zn1–O1	1.953(2)	Zn1–N1	2.011(3)
Zn1–O3C	2.220(3)	Zn2–O4	1.961(2)
Zn2–O7A	1.975(2)	Zn2–O5	1.990(3)
Zn2–N3B	2.011(2)		
O6C–Zn1–O3C	83.60(10)	N1–Zn1–O3C	88.00(11)
O6C–Zn1–O8C	83.95(11)	N1–Zn1–O8C	90.03(11)
O1–Zn1–O6C	103.32(11)	O4–Zn2–O7A	90.62(11)
O1–Zn1–O3C	86.58(11)	O4–Zn2–O5	135.60(11)
O1–Zn1–O8C	105.50(11)	O4–Zn2–N3B	103.38(10)
O1–Zn1–N1	135.50(11)	O7A–Zn2–O5	111.11(12)
O8C–Zn1–O3C	164.37(11)	O7A–Zn2–N3B	111.60(11)
N1–Zn1–O6C	119.88(11)	O5–Zn2–N3B	103.50(11)

symmetry code: A:  $3-x, 2-y, -z$ , B:  $2-x, 1-y, 1-z$  for MOF **1**; A:  $1-x, 2-y, 2-z$ ; B:  $x, 1+y, z$ ; C:  $2-x, 2-y, 2-z$  for

MOF **2**; A:  $1+x, y, z$ ; B:  $1+x, 1+y, z$ ; C:  $2-x, 1-y, 1-z$  for MOF **3**; A:  $1-x, -y, 1-z$ ; B:  $1-x, 1-y, 2-z$ ; C:  $1-x, 1-y,$

$1-z$  MOF **4**.

**Table S3** Thermal stability analysis for MOFs **1-4**

MOF	Loss of matter	Decomposition temperature/°C	Experimental value/%	Theoretical value/%
<b>1</b>	H <sub>2</sub> O/BETC <sup>4-</sup> and L1	150~200/250~521	8.45/80.63	8.54/80.75
<b>2</b>	H <sub>2</sub> O/BETC <sup>4-</sup> and L2	75~150/200~500	5.95/76.11	5.67/76.87
<b>3</b>	H <sub>2</sub> O/BETC <sup>4-</sup> and L3	82~160/310~520	4.25/77.99	5.01/77.16
<b>4</b>	H <sub>2</sub> O/BETC <sup>4-</sup> and L4	100~156/310~596	2.73/72.57	3.05/72.60

**Table S4.** The BET surface area and porosity of MOFs 1–4

MOF	BET surface area (m <sup>2</sup> /g)	Porosity (cm <sup>3</sup> /g)
MOF 1	11.339	0.0663
MOF 2	2.301	0.0198
MOF 3	8.608	0.0494
MOF 4	12.002	0.0664

**Table S5.** HOMO-LUMO energies (in eV) for MOF 1-4, L1-L4, H<sub>4</sub>BTEC and analytes

types	HOMO (eV)	LUMO (eV)
MOF 1	-4.990	-1.260
MOF 2	-4.971	-1.151
MOF 3	-4.980	-1.110
MOF 4	-5.014	-0.994
L1	-4.945	-0.855
L2	-5.120	-1.040
L3	-4.989	-1.169
L4	-5.045	-1.145
H <sub>4</sub> BTEC	-5.126	-1.626
acac	-4.931	-2.360
Fe <sup>3+</sup>	-25.677	-20.023

Figure Titles:

**Fig. S1.** The infrared spectrum of MOFs 1–4.

**Fig. S2.** TGA curves of MOFs 1–4.

**Fig. S3.** The PXRD pattern of the bulk sample is consistent with the simulated pattern of the single crystal structure in MOFs 1–4.

**Fig. S4.** PXRD patterns of MOFs 1-4 under simulated conditions.

**Fig. S5.** The change of the fluorescence emission intensity of MOFs 1-4 in different pH solutions.

**Fig. S6.** (a) In MOF 1, the two-dimensional structure formation process; (b) In MOF 1, the simplification of BETC<sup>4-</sup> and L ligand and the specific formation process of topological structure.

**Fig. S7.** (a) In MOF 2, the two-dimensional structure formation process; (b) In MOF 2, the simplification of BETC<sup>4-</sup> and L ligand and the specific formation process of topological structure.

**Fig. S8.** (a) In MOF 3, the three-dimensional structure formation process; (b) In MOF 3, the simplification of BETC<sup>4-</sup> and L ligand and the specific formation process of topological structure

**Fig. S9.** (a) In MOF 4, the three-dimensional structure formation process; (b) In MOF 4, the simplification of BETC<sup>4-</sup> and L ligand and the specific formation process of topological structure

**Fig. S10.** View of the coordination modes of L1-L4 ligands in MOFs 1–4.

**Fig. S11.** Solid-state emission spectra of ligands L1–L4 and H<sub>4</sub>BETC at room temperature.

**Fig. S12.** (a) Photoluminescence intensities of MOF 2 introduced into organic solvents at room temperature,  $\lambda_{\text{ex}} = 289 \text{ nm}$ ; (b) Influence of interfering organic solvents on the luminescence intensity of acac at room temperature in MOF 2,  $\lambda_{\text{ex}} = 289 \text{ nm}$ ; (c) Fluorescence emission intensity at different concentrations (0–100  $\mu\text{L}$ , the corresponding concentration are 0–7.6  $\mu\text{mol/L}$ ) of acac using H<sub>2</sub>O as the system in MOF 2,  $\lambda_{\text{ex}} = 289 \text{ nm}$ ; (d) Relationship between  $I_0/I-1$  and different concentration of acac ( $I_0$  and  $I$  refer to the luminescent intensity of MOF 2 without and with acac, respectively). Inset: linear plot of  $I_0/I-1$  and low acac concentration of MOF 2.

**Fig. S13.** (a) Photoluminescence intensities of MOF 3 introduced into organic solvents at room temperature,  $\lambda_{\text{ex}} = 305 \text{ nm}$ ; (b) Influence of interfering organic solvents on the luminescence intensity of acac at room temperature in MOF 2,  $\lambda_{\text{ex}} = 305 \text{ nm}$ ; (c) Fluorescence emission intensity at different concentrations (0–100  $\mu\text{L}$ , the corresponding concentration are 0–7.6  $\mu\text{mol/L}$ ) of acac using H<sub>2</sub>O as the system in MOF 3,  $\lambda_{\text{ex}} = 305 \text{ nm}$ ; (d) Relationship between  $I_0/I-1$  and different

concentration of acac ( $I_0$  and  $I$  refer to the luminescent intensity of MOF **3** without and with acac, respectively). Inset: linear plot of  $I_0/I-1$  and low acac concentration of MOF **3**.

**Fig. S14.** (a) Photoluminescence intensities of MOF **4** introduced into organic solvents at room temperature,  $\lambda_{\text{ex}} = 311$  nm; (b) Influence of interfering organic solvents on the luminescence intensity of acac at room temperature in MOF **4**,  $\lambda_{\text{ex}} = 311$  nm; (c) Fluorescence emission intensity at different concentrations (0–100  $\mu\text{L}$ , the corresponding concentration are 0–7.6  $\mu\text{mol/L}$ ) of acac using  $\text{H}_2\text{O}$  as the system in MOF **4**,  $\lambda_{\text{ex}} = 311$  nm; (d) Relationship between  $I_0/I-1$  and different concentration of acac ( $I_0$  and  $I$  refer to the luminescent intensity of MOF **4** without and with acac, respectively). Inset: linear plot of  $I_0/I-1$  and low acac concentration of MOF **4**.

**Fig. S15.** The time required for the quenching efficiency of acac to reach the maximum in MOFs **1-4**.

**Fig. S16.** (a) Luminescence spectra of MOF **2** with different metal ions ( $10^{-4}$  M) in EtOH/ $\text{H}_2\text{O}$  (1:1, v/v) solutions at 289 nm. (b) Influence of interfering ions on the luminescence intensity of  $\text{Fe}^{3+}$  ions at room temperature in EtOH/ $\text{H}_2\text{O}$  (1:1, v/v) solutions,  $\lambda_{\text{ex}} = 289$  nm. (c) Liquid emission spectra of MOF **2** as a result of different concentrations of  $\text{Fe}^{3+}$  ions at room temperature in EtOH/ $\text{H}_2\text{O}$  (1:1, v/v) solutions,  $\lambda_{\text{ex}} = 289$  nm. (d) Plot of relative intensity vs.  $\text{Fe}^{3+}$  ions concentration.

**Fig. S17.** (a) Luminescence spectra of MOF **3** with different metal ions ( $10^{-4}$  M) in EtOH/ $\text{H}_2\text{O}$  (1:1, v/v) solutions at 305 nm. (b) Influence of interfering ions on the luminescence intensity of  $\text{Fe}^{3+}$  ions at room temperature in EtOH/ $\text{H}_2\text{O}$  (1:1, v/v) solutions,  $\lambda_{\text{ex}} = 305$  nm. (c) Liquid emission spectra of MOF **3** as a result of different concentrations of  $\text{Fe}^{3+}$  ions at room temperature in EtOH/ $\text{H}_2\text{O}$  (1:1, v/v) solutions,  $\lambda_{\text{ex}} = 305$  nm. (d) Plot of relative intensity vs.  $\text{Fe}^{3+}$  ions concentration.

**Fig. S18.** (a) Luminescence spectra of MOF **4** with different metal ions ( $10^{-4}$  M) in EtOH/ $\text{H}_2\text{O}$  (1:1, v/v) solutions at 311 nm. (b) Influence of interfering ions on the luminescence intensity of  $\text{Fe}^{3+}$  ions at room temperature in EtOH/ $\text{H}_2\text{O}$  (1:1, v/v) solutions,  $\lambda_{\text{ex}} = 311$  nm. (c) Liquid emission spectra of MOF **4** as a result of different concentrations of  $\text{Fe}^{3+}$  ions at room temperature in EtOH/ $\text{H}_2\text{O}$  (1:1, v/v) solutions,  $\lambda_{\text{ex}} = 311$  nm. (d) Plot of relative intensity vs.  $\text{Fe}^{3+}$  ions concentration.

**Fig. S19.** The time required for the quenching efficiency of  $\text{Fe}^{3+}$  ions to reach the maximum in

MOFs **1-4**.

**Fig. S20.** (a) Liquid emission spectra of L1 ligand as a result of different concentrations of  $\text{Fe}^{3+}$  ions at room temperature in EtOH/ $\text{H}_2\text{O}$  (1:1, v/v) solutions;(b) Fluorescence emission intensity at different concentrations of acac using  $\text{H}_2\text{O}$  as the system in L1 ligand,  $\lambda_{\text{ex}} = 298$  nm.

**Fig. S21.** (a) Liquid emission spectra of  $\text{H}_4\text{BTEC}$  ligand as a result of different concentrations of  $\text{Fe}^{3+}$  ions at room temperature in EtOH/ $\text{H}_2\text{O}$  (1:1, v/v) solutions;(b) Fluorescence emission intensity at different concentrations of acac using  $\text{H}_2\text{O}$  as the system in L1 ligand,  $\lambda_{\text{ex}} = 310$  nm.

**Fig. S22.** Comparison of the quenching efficiency of MOFs **1-4** for sensing acac/ $\text{Fe}^{3+}$  over four cycles.

**Fig. S23.** PXRD patterns of MOFs **1-4** after 4 cycles of detecting  $\text{Fe}^{3+}$  or acac

**Fig. S24.** (a) Effects of pH on the fluorescence maxima of MOFs **1-4** + acac and MOFs **1-4** +  $\text{Fe}^{3+}$ .

**Fig. S25.** (a) TEM image of MOF **2**, (b) TEM elemental mapping images of C, O, N, Zn and Fe in MOF **2**

**Fig. S26.** (a) TEM image of MOF **3**, (b) TEM elemental mapping images of C, O, N, Zn and Fe in MOF **3**

**Fig. S27.** (a) TEM image of MOF **3**, (b) TEM elemental mapping images of C, O, N, Zn and Fe in MOF **4**

**Fig. S28.** (a) HOMO and LUMO energy levels for MOFs **1-4**, L1-L4,  $\text{H}_4\text{BTEC}$  ligands and acac; (b) HOMO and LUMO energy levels for  $\text{Fe}^{3+}$ .

**Fig. S29.** Spectral overlap between the absorption spectra of acac ions and the excitation spectra of MOFs **1-4**.

**Fig. S30.** Spectral overlap between the absorption spectra of  $\text{Fe}^{3+}$  ions and the excitation spectra of MOFs **1-4**.

**Fig. S31.** (a) View of the coordination environment of  $\text{Zn}^{\text{II}}$  in MOF **2** with the ellipsoids drawn at the 30% probability level (H atoms are omitted for clarity, symmetry code: symmetry code: A:  $1-x, 2-y, 2-z$ ; B:  $x, 1+y, z$ ; C =  $2-x, 2-y, 2-z$ ; D:  $-x, 1-y, 2-z$ ); (b) the ladder chain  $[\text{Zn}_4(\text{L2})]_n$  was formed by L2 ligands and  $\text{Zn}^{\text{II}}$  atoms, the  $\text{BTEC}^{4-}$  anions create a 1D infinite  $\text{Zn}_4(\text{BTEC})_n$  chain by linking adjacent  $\text{Zn}^{\text{II}}$  atoms in MOF **2**; (c) in MOF **2**, the two structures,  $[\text{Zn}_4(\text{L2})]_n$  and  $\text{Zn}_4(\text{BTEC})_n$ , are cross-linked into 2D network structures in different directions; (d) a rare 2D

structure with the **4,4,4L10** topology (cyan spheres:  $\text{Zn}^{\text{II}}$  atoms ; red spheres:  $\text{BTEC}^{4-}$  anions ; blue spheres: L2 ligands).

**Fig. S32.** (a) View of the coordination environment of  $\text{Zn}^{\text{II}}$  in MOF **4** with the ellipsoids drawn at the 30% probability level (H atoms are omitted for clarity, symmetry code: A:  $1-x, -y, 1-z$ ; B:  $1-x, 1-y, 2-z$ ; C:  $1-x, 1-y, 1-z$ ; D:  $2-x, 1-y, 1-z$ ; E:  $-x, -y, 1-z$ ; F:  $1-x, 2-y, 2-z$ ); (b) The 2D  $[(\text{Zn}_{10}(\text{BTEC})_2)_n]$  network network formed by  $\text{Zn}^{\text{II}}$  and  $\text{BTEC}^{4-}$  ligands in MOF **4** and one  $[\text{Zn}_4(\text{L4})]$  unit with the surrounding  $\text{Zn}^{\text{II}}$  atoms in MOF **4**; (c) a 3D layer structure formed by  $[\text{Zn}_4(\text{L4})]$  units and  $[(\text{Zn}_{10}(\text{BTEC})_2)_n]$  network; (d) A rare (4,4,4,6,6)-connected 3D structure with the **4,4,4,6,6T3** topology in MOF **3** (cyan spheres:  $\text{Zn}^{\text{II}}$  atoms; red spheres:  $\text{BTEC}^{4-}$  anions; blue spheres: L4 ligands).

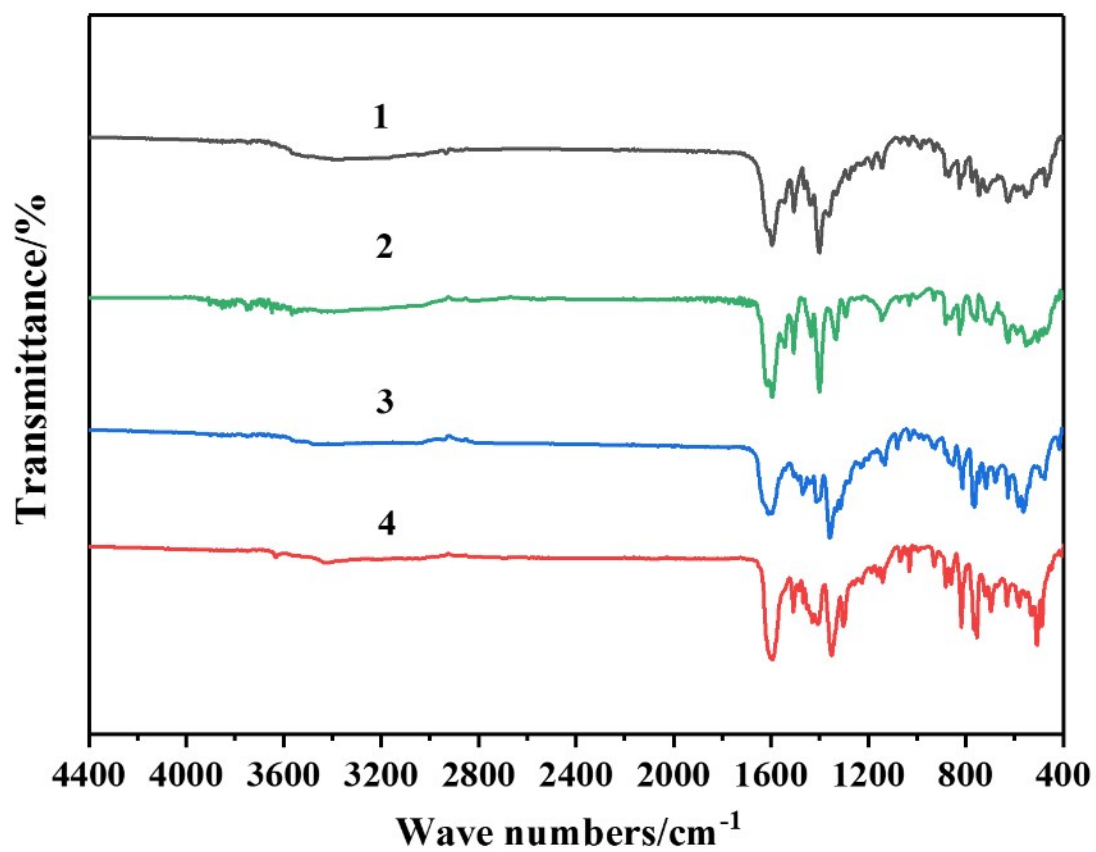


Fig. S1. The infrared spectrum of MOFs 1-4.

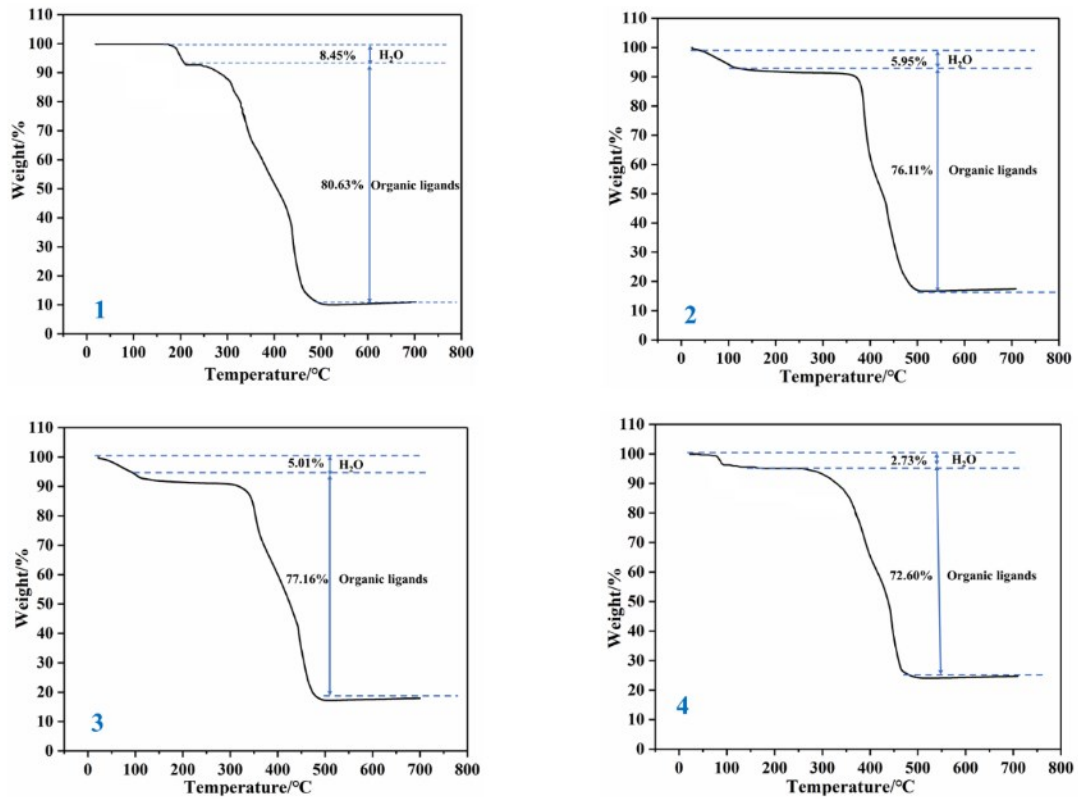
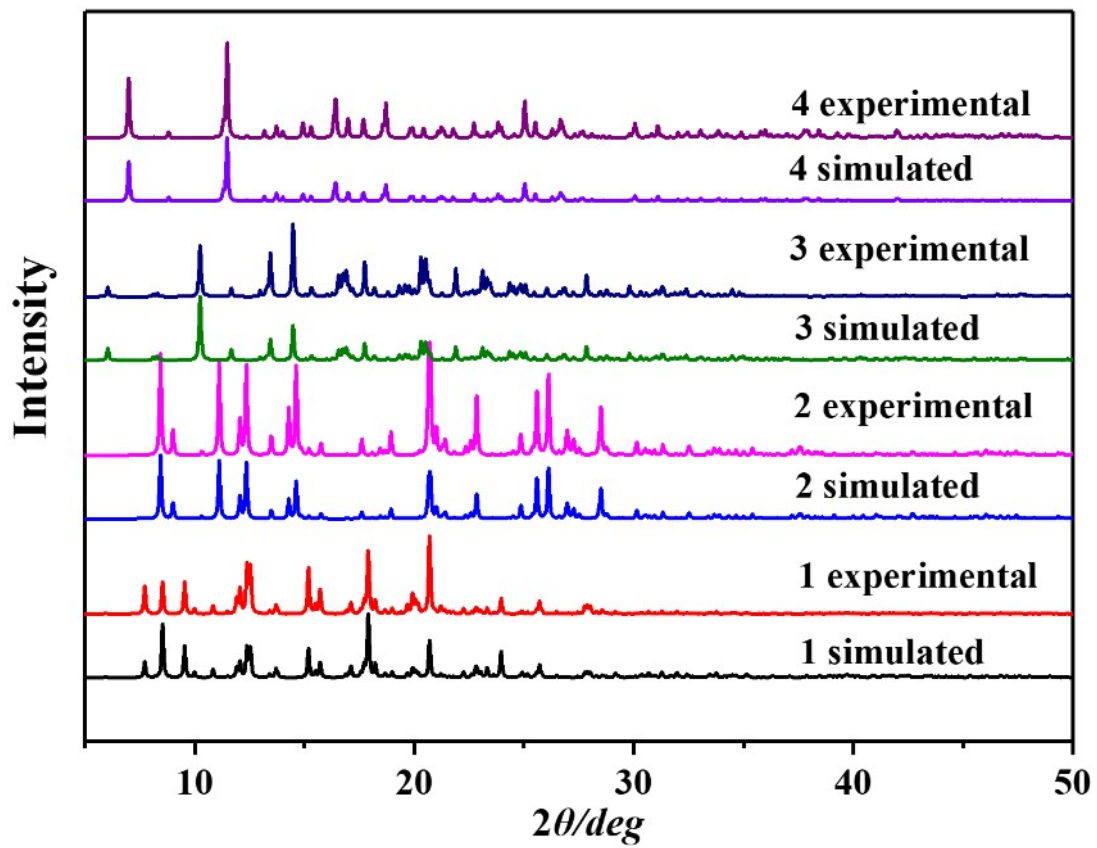


Fig. S2. TGA curves of MOFs 1-4.



**Fig. S3.** The PXR D pattern of the bulk sample is consistent with the simulated pattern of the single crystal structure in MOFs 1–4.

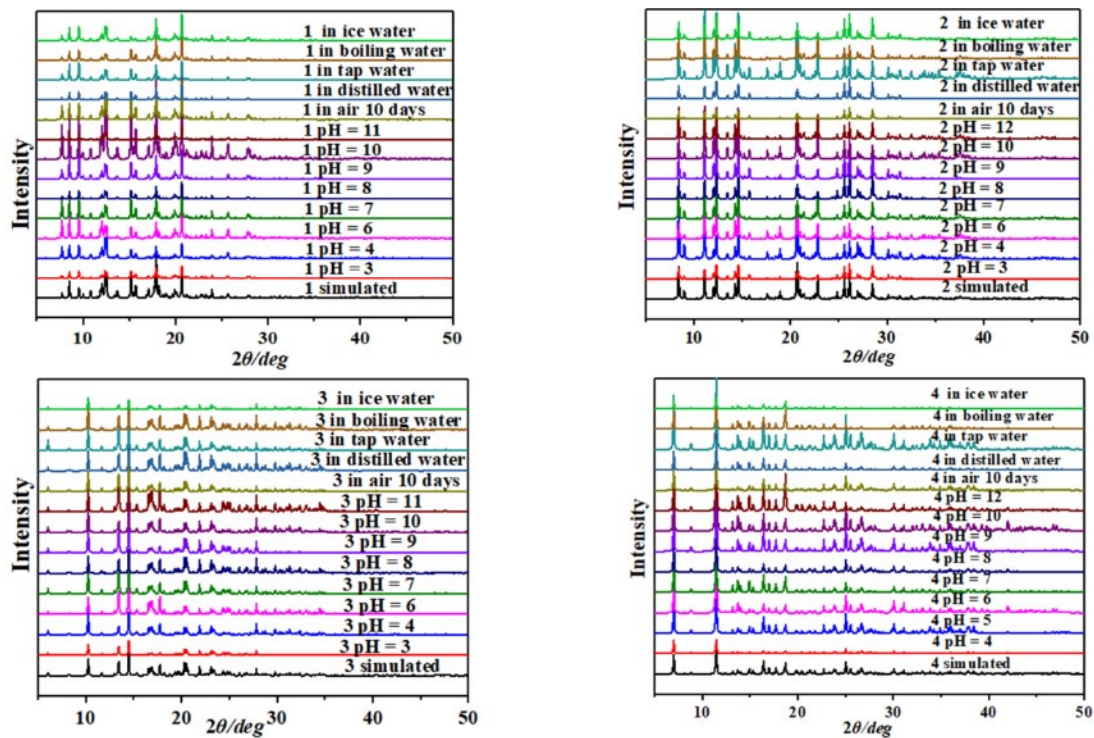
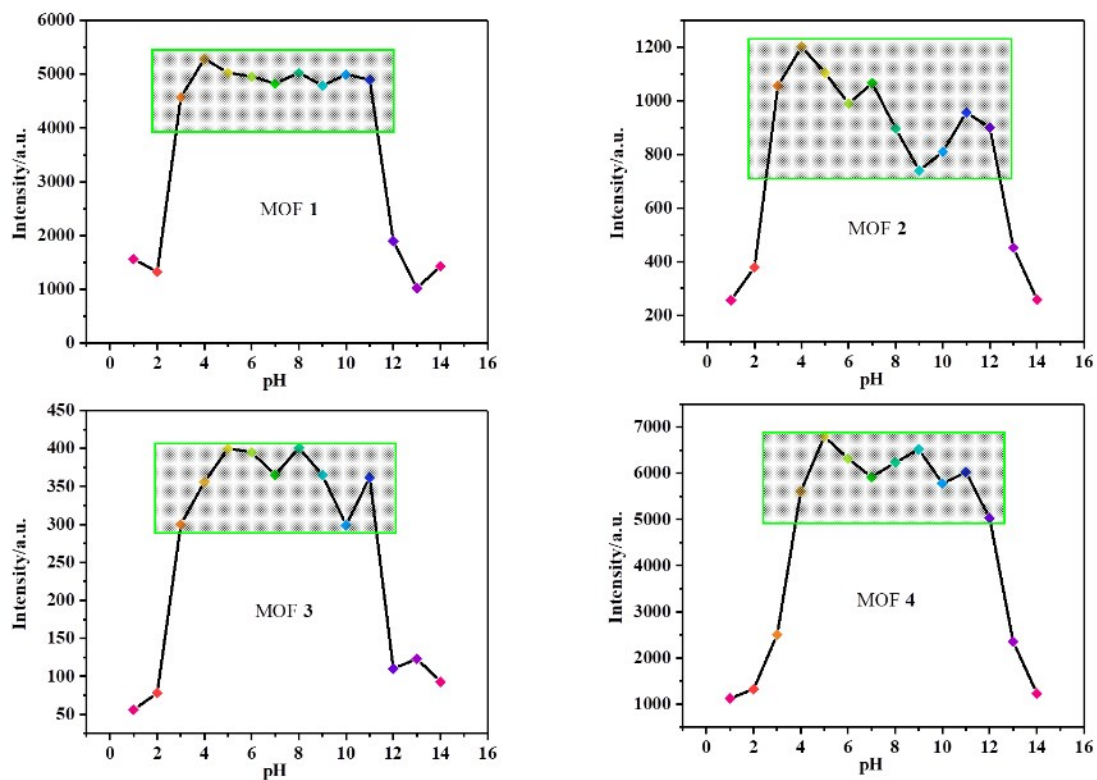
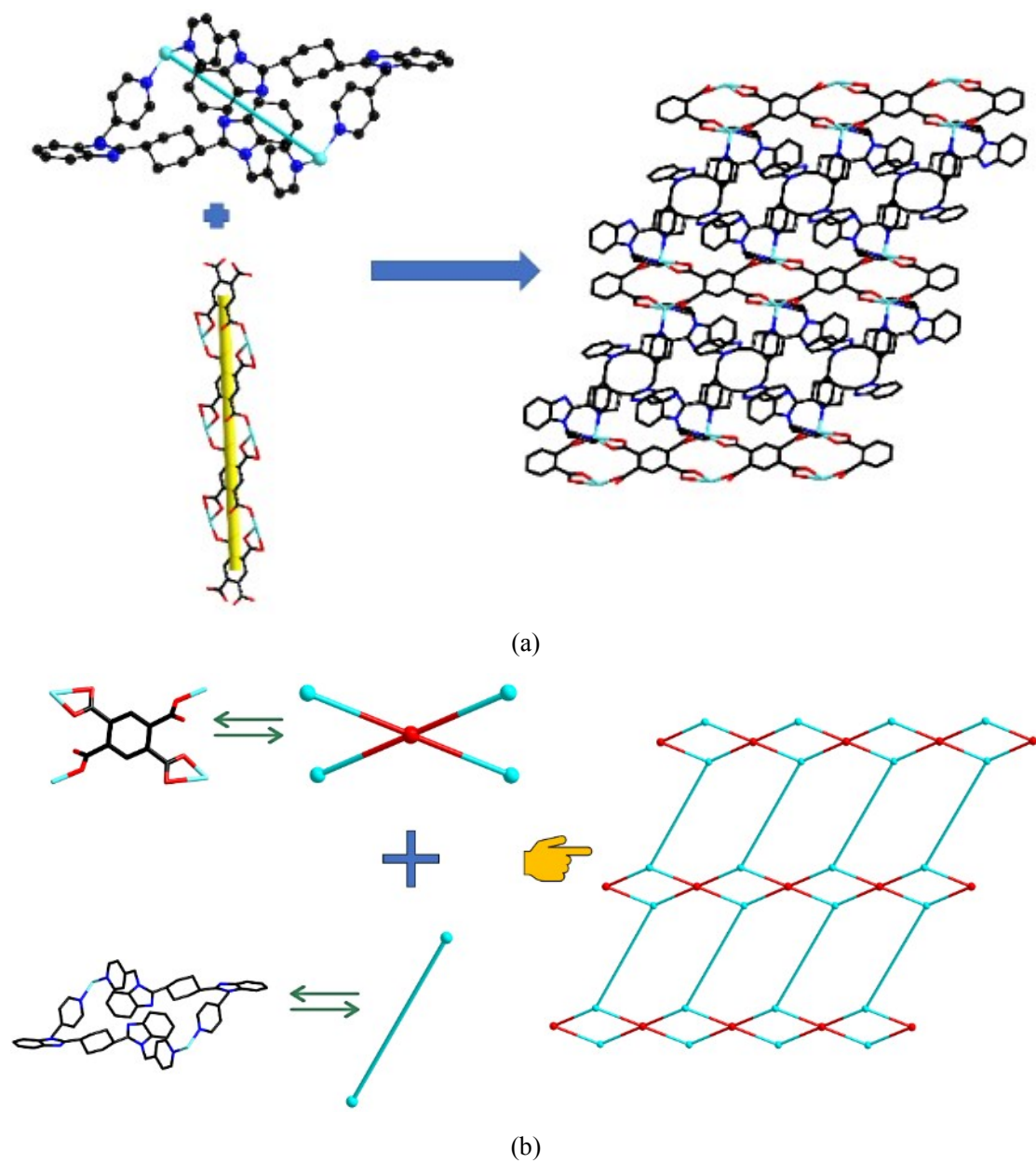


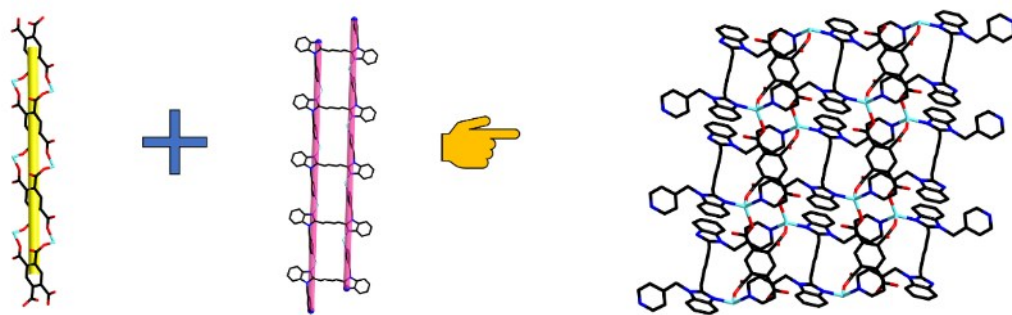
Fig. S4. PXRD patterns of MOFs 1-4 under simulated conditions.



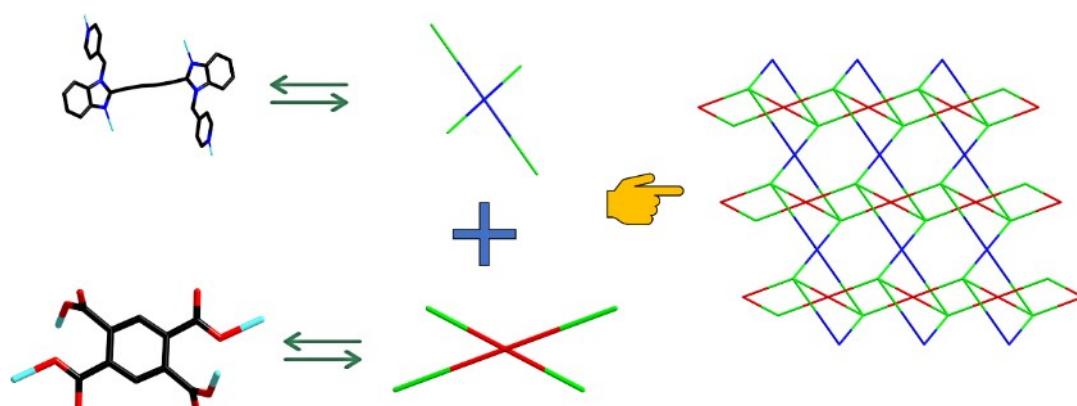
**Fig. S5.** The change of the fluorescence emission intensity of MOFs 1-4 in different pH solutions.



**Fig. S6.** (a) In MOF **1**, the two-dimensional structure formation process; (b) In MOF **1**, the simplification of BETC<sup>4+</sup> and L ligand and the specific formation process of topological structure.



(a)



(b)

**Fig. S7.** (a) In MOF **2**, the two-dimensional structure formation process; (b) In MOF **2**, the simplification of  $\text{BETC}^{4-}$  and L ligand and the specific formation process of topological structure.

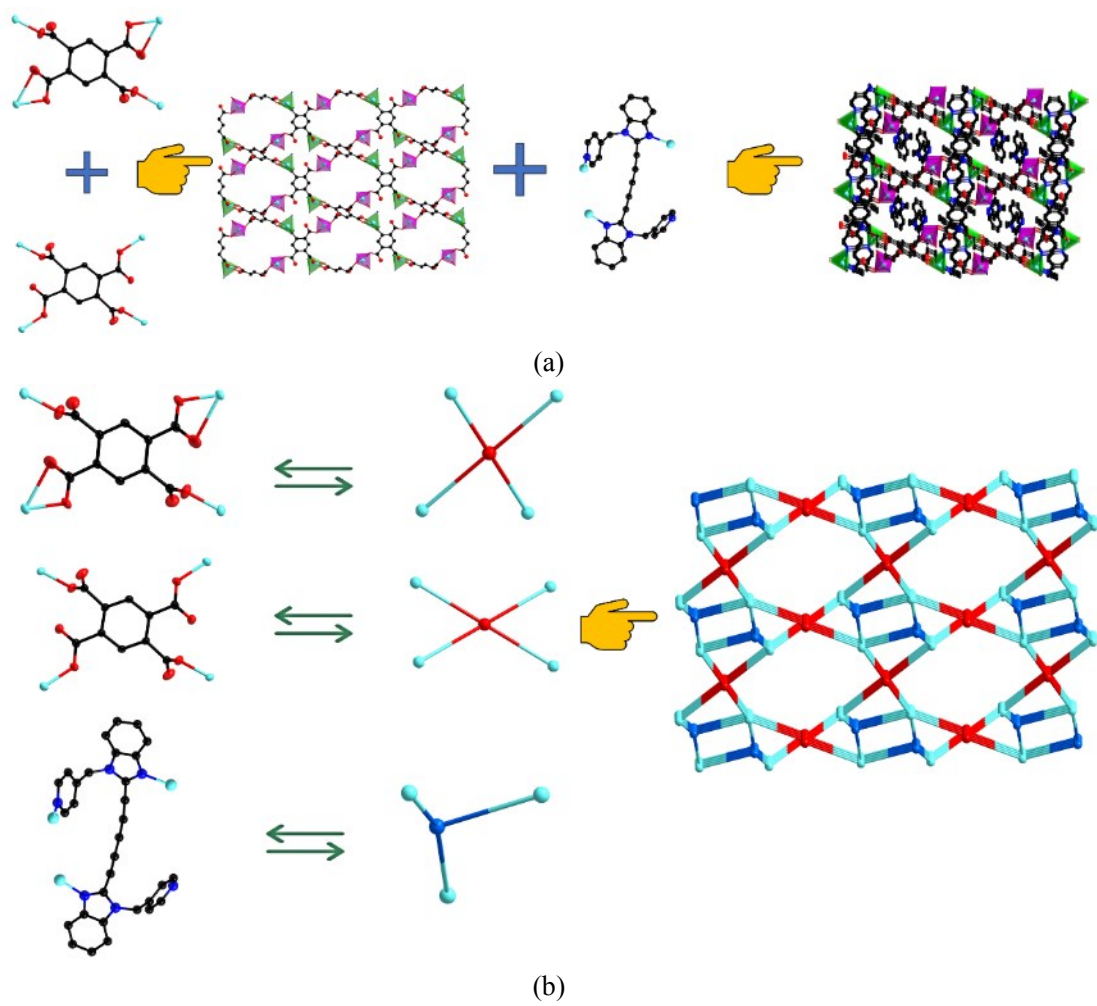
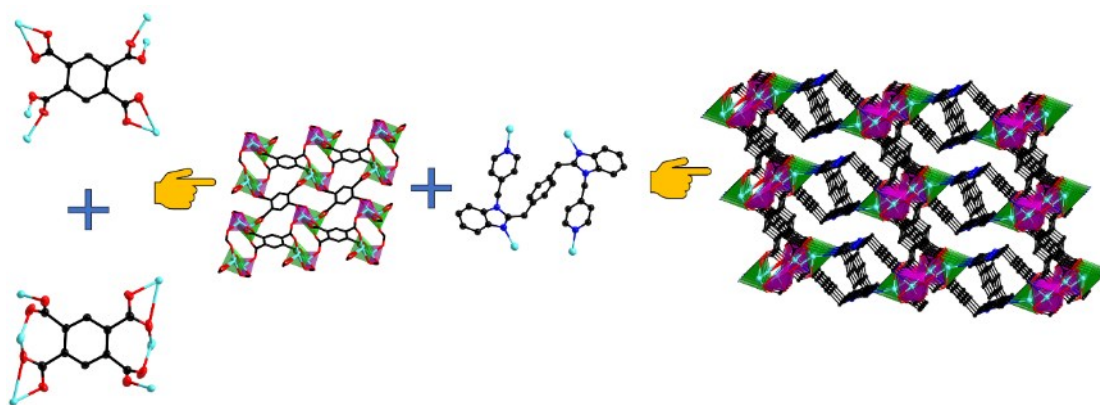
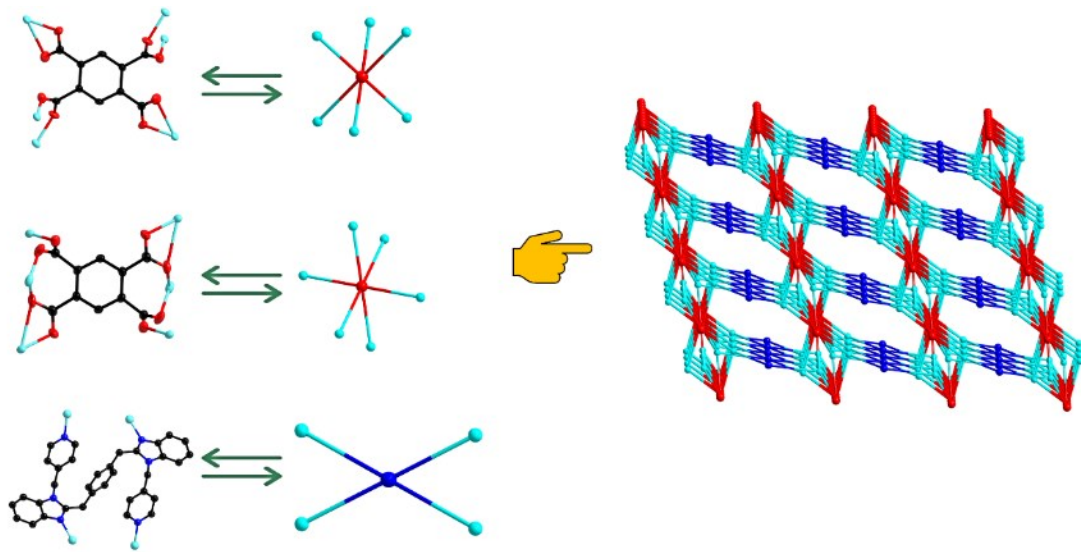


**Fig. S8.** (a) In MOF 3, the three-dimensional structure formation process; (b) In MOF 3, the simplification of  $\text{BETC}^{4+}$  and L ligand and the specific formation process of topological structure

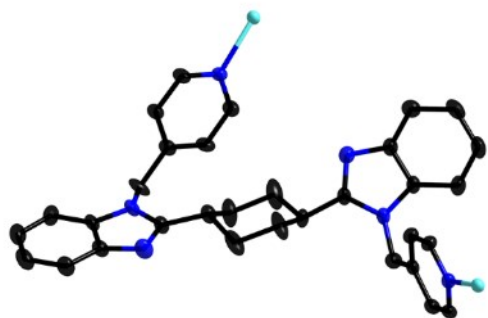


(a)

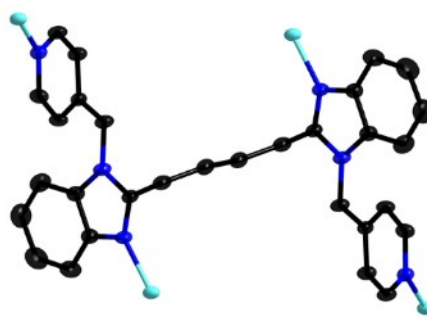


(b)

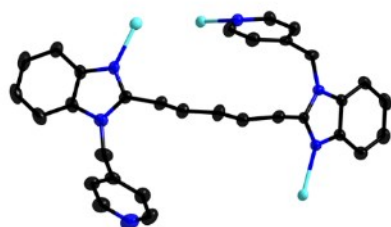
**Fig. S9.** (a) In MOF 4, the three-dimensional structure formation process; (b) In MOF 4, the simplification of BETC<sup>4-</sup> and L ligand and the specific formation process of topological structure



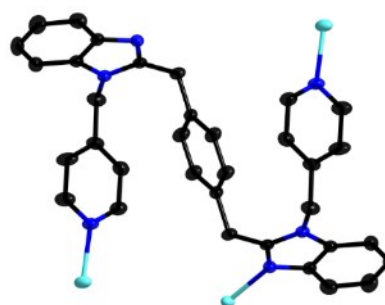
MOF 1



MOF 2



MOF 3



MOF 4

**Fig. S10.** View of the coordination modes of L1-L4 ligands in MOFs 1-4.

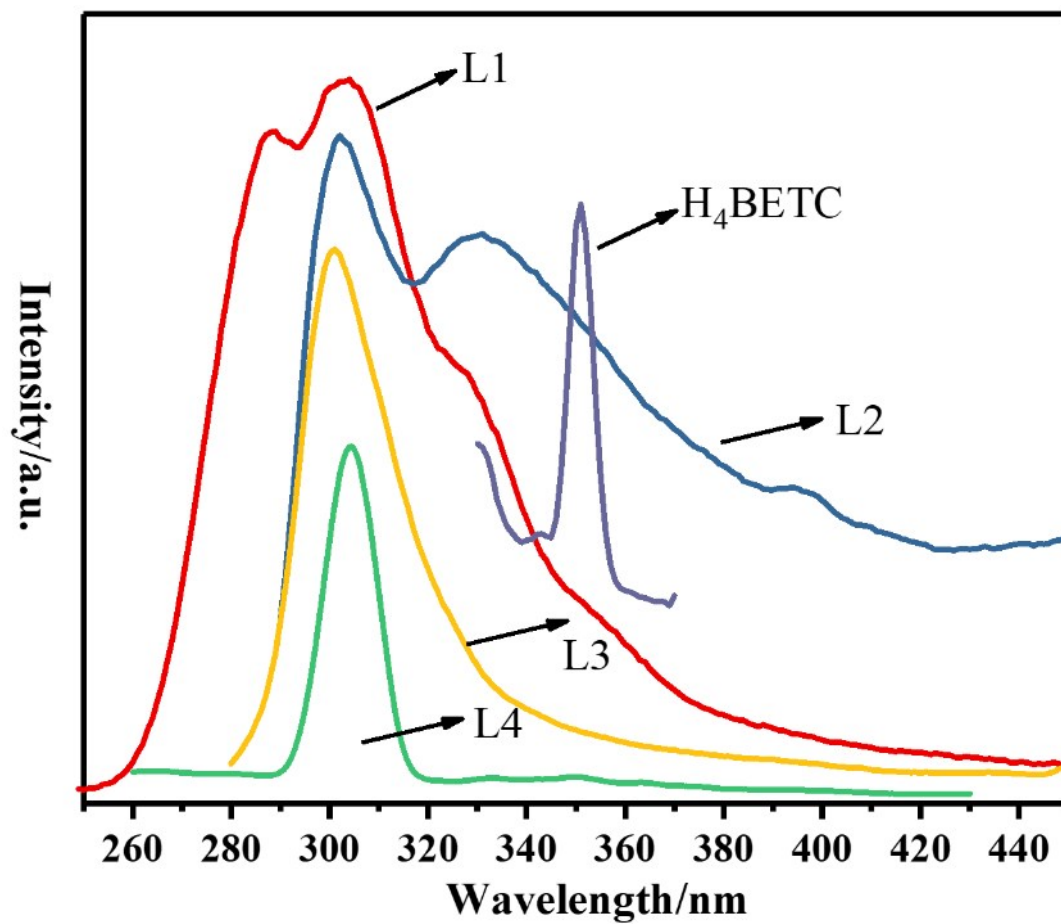
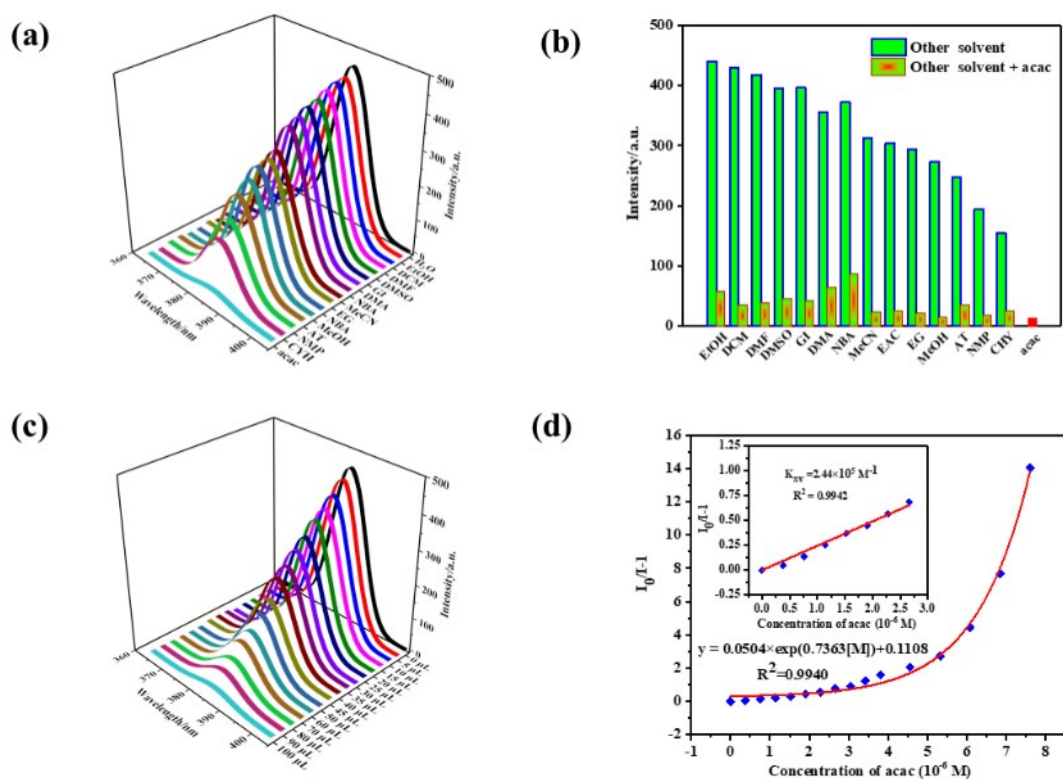
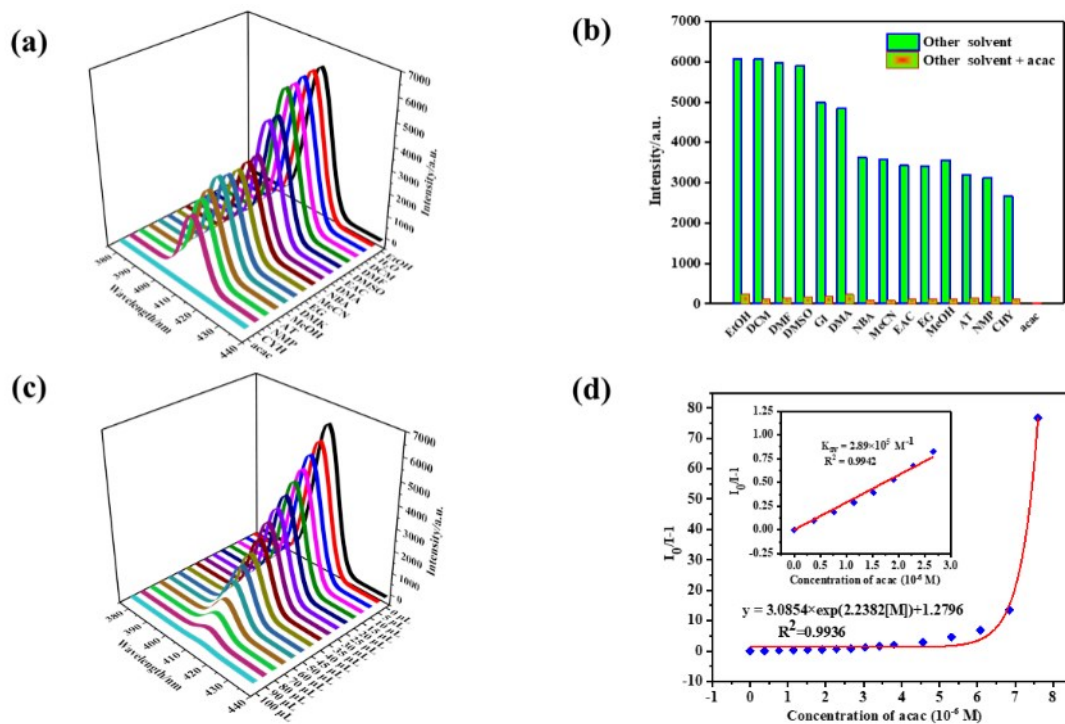


Fig. S11. Solid-state emission spectra of ligands L1–L4 and H<sub>4</sub>BETC at room temperature.





**Fig. S13.** (a) Photoluminescence intensities of MOF 3 introduced into organic solvents at room temperature,  $\lambda_{\text{ex}} = 305 \text{ nm}$ ; (b) Influence of interfering organic solvents on the luminescence intensity of acac at room temperature in MOF 2,  $\lambda_{\text{ex}} = 305 \text{ nm}$ ; (c) Fluorescence emission intensity at different concentrations (0–100  $\mu$ L, the corresponding concentration are 0–7.6  $\mu$ mol/L) of acac using H<sub>2</sub>O as the system in MOF 3,  $\lambda_{\text{ex}} = 305 \text{ nm}$ ; (d) Relationship between  $I_0/I-1$  and different concentration of acac ( $I_0$  and  $I$  refer to the luminescent intensity of MOF 3 without and with acac, respectively). Inset: linear plot of  $I_0/I-1$  and low acac concentration of MOF 3.



**Fig. S14.** (a) Photoluminescence intensities of MOF 4 introduced into organic solvents at room temperature,  $\lambda_{\text{ex}} = 311 \text{ nm}$ ; (b) Influence of interfering organic solvents on the luminescence intensity of acac at room temperature in MOF 4,  $\lambda_{\text{ex}} = 311 \text{ nm}$ ; (c) Fluorescence emission intensity at different concentrations (0–100  $\mu\text{L}$ , the corresponding concentration are 0–7.6  $\mu\text{mol/L}$ ) of acac using H<sub>2</sub>O as the system in MOF 4,  $\lambda_{\text{ex}} = 311 \text{ nm}$ ; (d) Relationship between  $I_0/I-1$  and different concentration of acac ( $I_0$  and  $I$  refer to the luminescent intensity of MOF 4 without and with acac, respectively). Inset: linear plot of  $I_0/I-1$  and low acac concentration of MOF 4.

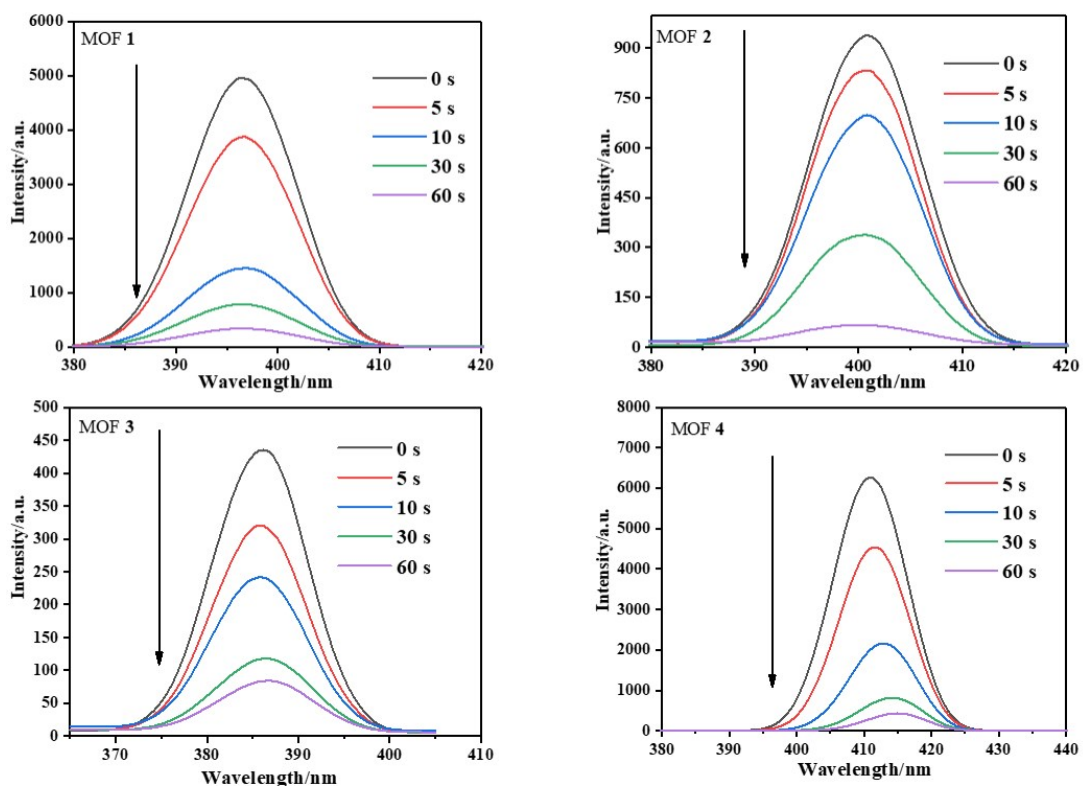


**Fig. S15.** The time required for the quenching efficiency of acac to reach the maximum in MOFs

1-4.

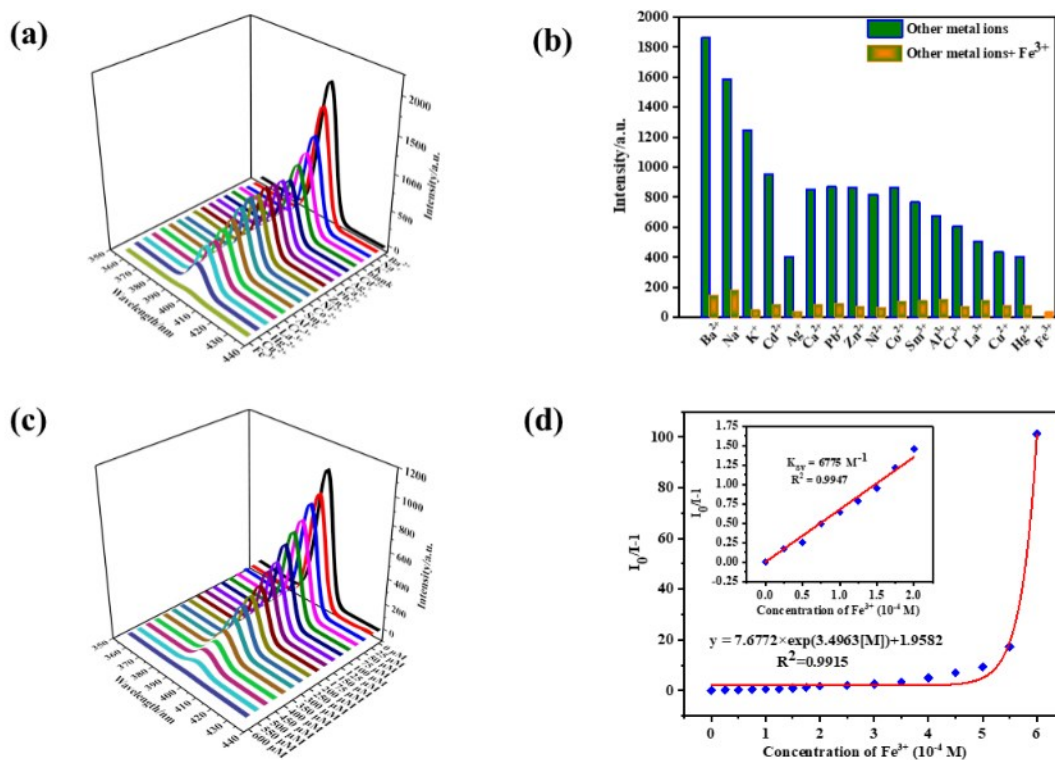


**Fig. S16.** (a) Luminescence spectra of MOF 2 with different metal ions ( $10^{-4}$  M) in EtOH/H<sub>2</sub>O (1:1, v/v) solutions at 289 nm. (b) Influence of interfering ions on the luminescence intensity of Fe<sup>3+</sup> ions at room temperature in EtOH/H<sub>2</sub>O (1:1, v/v) solutions,  $\lambda_{ex} = 289$  nm. (c) Liquid emission spectra of MOF 2 as a result of different concentrations of Fe<sup>3+</sup> ions at room temperature in EtOH/H<sub>2</sub>O (1:1, v/v) solutions,  $\lambda_{ex} = 289$  nm. (d) Plot of relative intensity vs. Fe<sup>3+</sup> ions concentration.

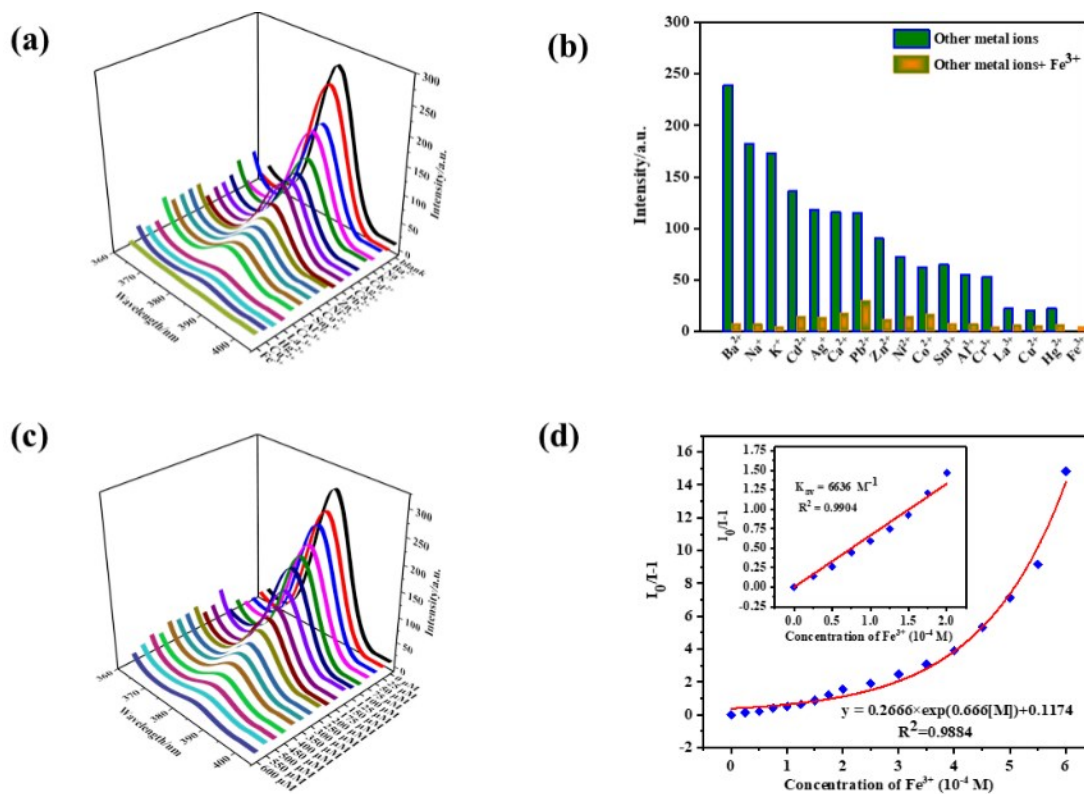


**Fig. S17.** (a) Luminescence spectra of MOF **3** with different metal ions (10<sup>-4</sup> M) in EtOH/H<sub>2</sub>O (1:1, v/v) solutions at 305 nm. (b) Influence of interfering ions on the luminescence intensity of Fe<sup>3+</sup> ions at room temperature in EtOH/H<sub>2</sub>O (1:1, v/v) solutions, λ<sub>ex</sub> = 305 nm. (c) Liquid emission spectra of MOF **3** as a result of different concentrations of Fe<sup>3+</sup> ions at room temperature in EtOH/H<sub>2</sub>O (1:1, v/v) solutions, λ<sub>ex</sub> = 305 nm. (d) Plot of relative intensity vs. Fe<sup>3+</sup> ions concentration.

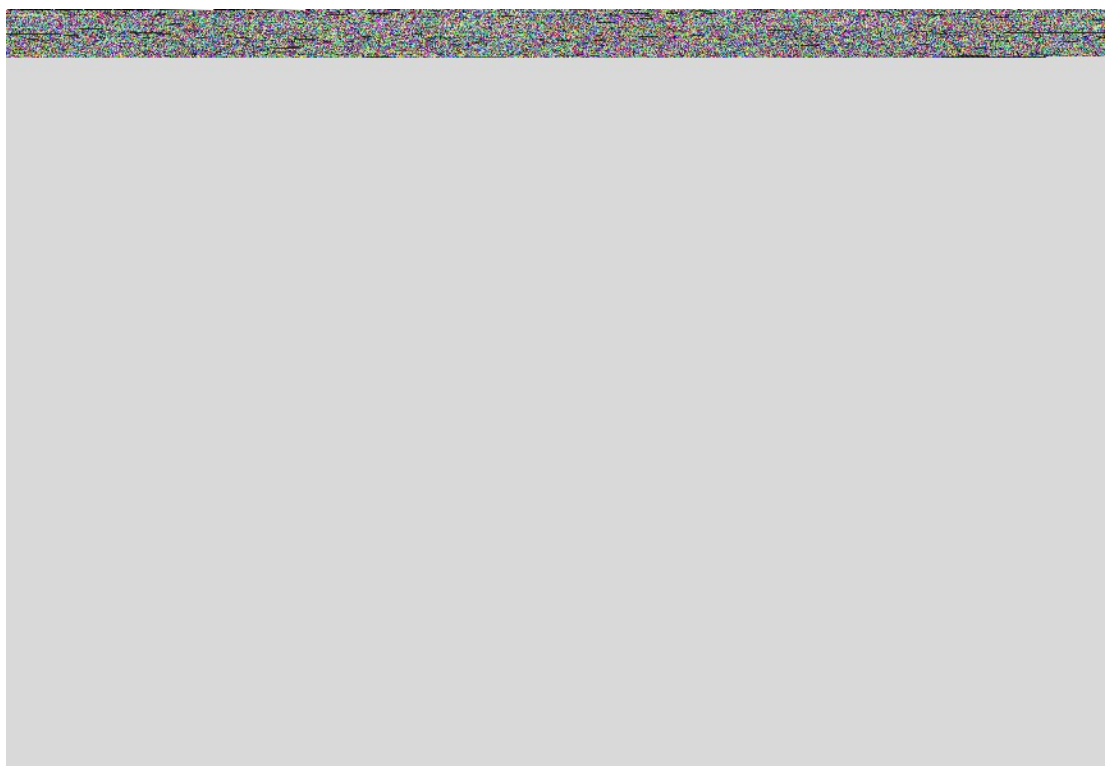


**Fig. S18.** (a) Luminescence spectra of MOF **4** with different metal ions ( $10^{-4}$  M) in EtOH/H<sub>2</sub>O (1:1, v/v) solutions at 311 nm. (b) Influence of interfering ions on the luminescence intensity of Fe<sup>3+</sup> ions at room temperature in EtOH/H<sub>2</sub>O (1:1, v/v) solutions,  $\lambda_{\text{ex}} = 311$  nm. (c) Liquid emission spectra of MOF **4** as a result of different concentrations of Fe<sup>3+</sup> ions at room temperature in EtOH/H<sub>2</sub>O (1:1, v/v) solutions,  $\lambda_{\text{ex}} = 311$  nm. (d) Plot of relative intensity vs. Fe<sup>3+</sup> ions concentration.

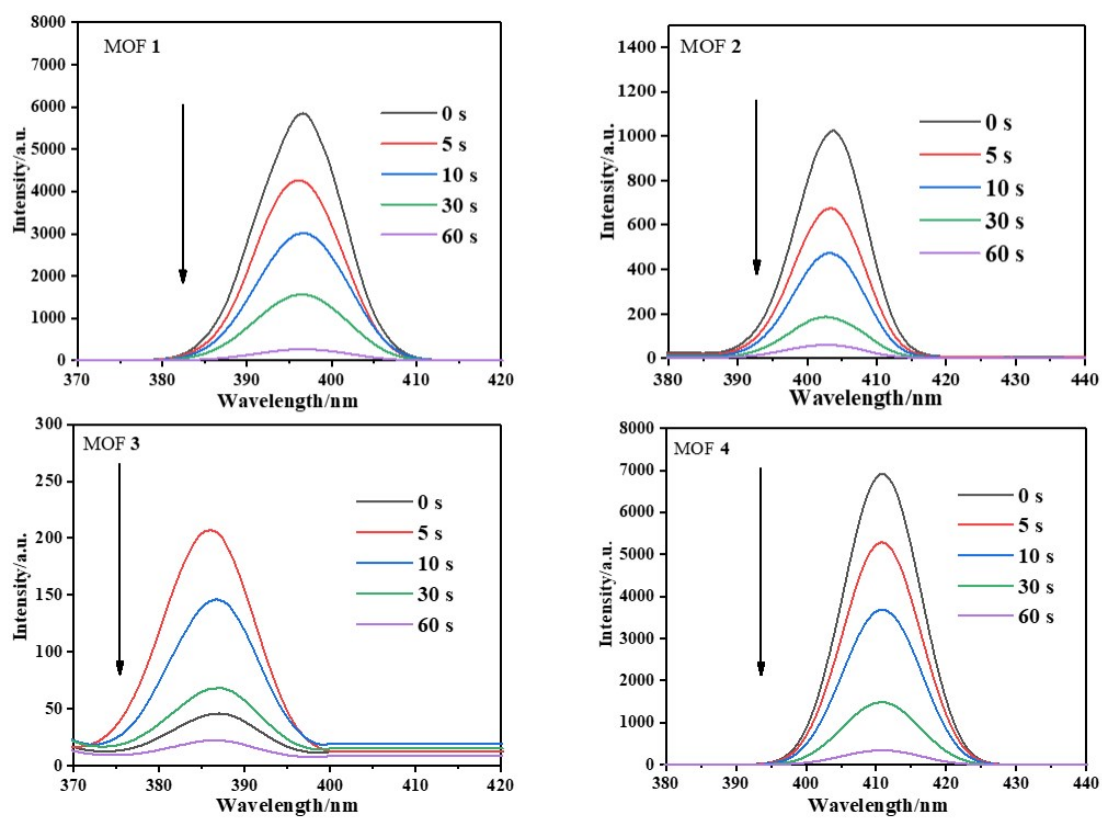


**Fig. S19.** The time required for the quenching efficiency of  $\text{Fe}^{3+}$  ions to reach the maximum in MOFs 1-4.

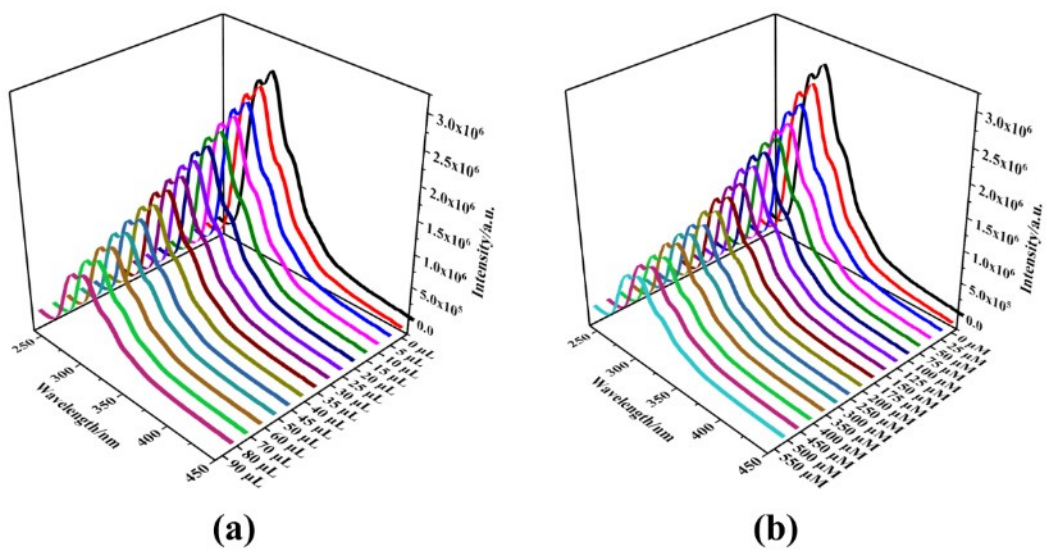


**Fig. S20.** (a) Liquid emission spectra of L1 ligand as a result of different concentrations of  $\text{Fe}^{3+}$  ions at room temperature in EtOH/ $\text{H}_2\text{O}$  (1:1, v/v) solutions; (b) Fluorescence emission intensity at different concentrations of acac using  $\text{H}_2\text{O}$  as the system in L1 ligand,  $\lambda_{\text{ex}} = 298$  nm.

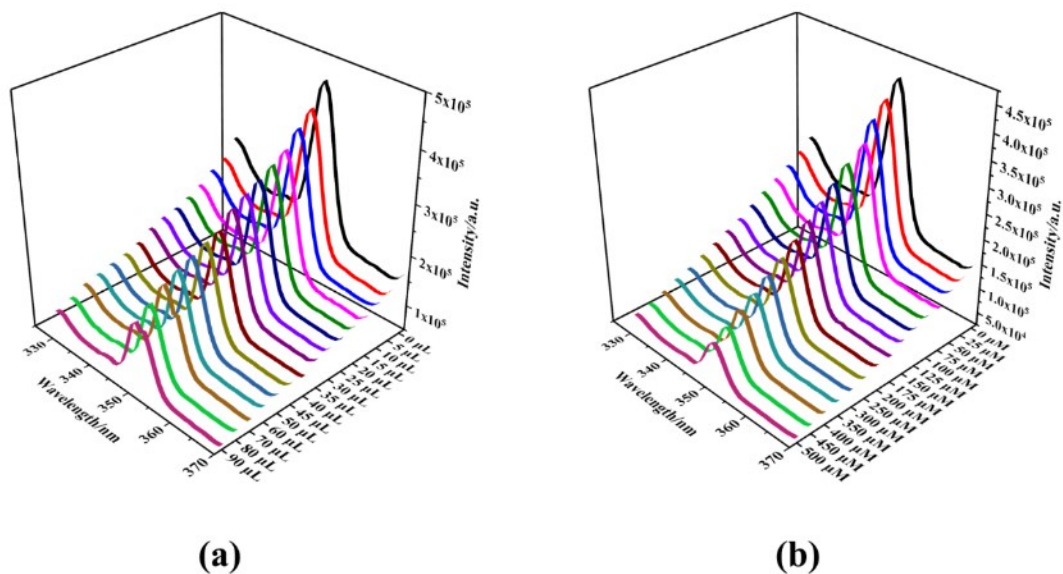


**Fig. S21.** (a) Liquid emission spectra of H<sub>4</sub>BTEC ligand as a result of different concentrations of Fe<sup>3+</sup> ions at room temperature in EtOH/H<sub>2</sub>O (1:1, v/v) solutions;(b) Fluorescence emission intensity at different concentrations of acac using H<sub>2</sub>O as the system in L1 ligand,  $\lambda_{\text{ex}} = 310 \text{ nm}$ .

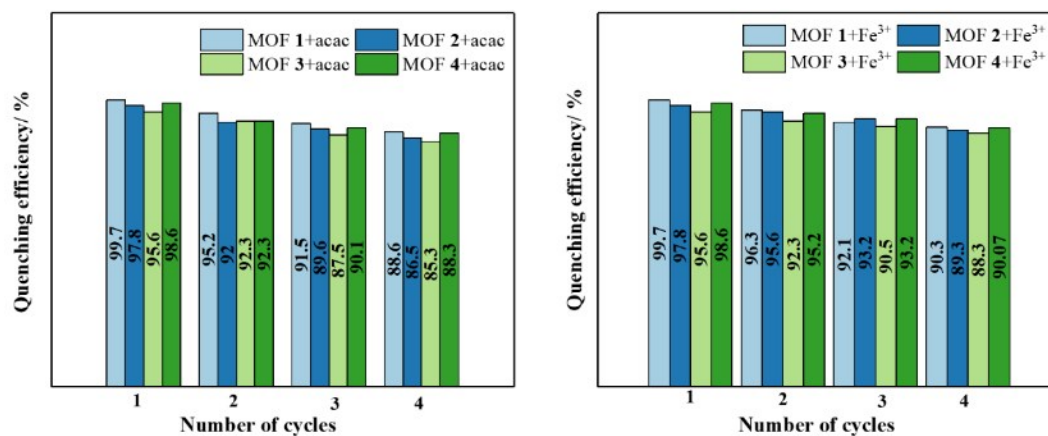


**Fig. S22.** Comparison of the quenching efficiency of MOFs **1-4** for sensing acac/Fe<sup>3+</sup> over four cycles.

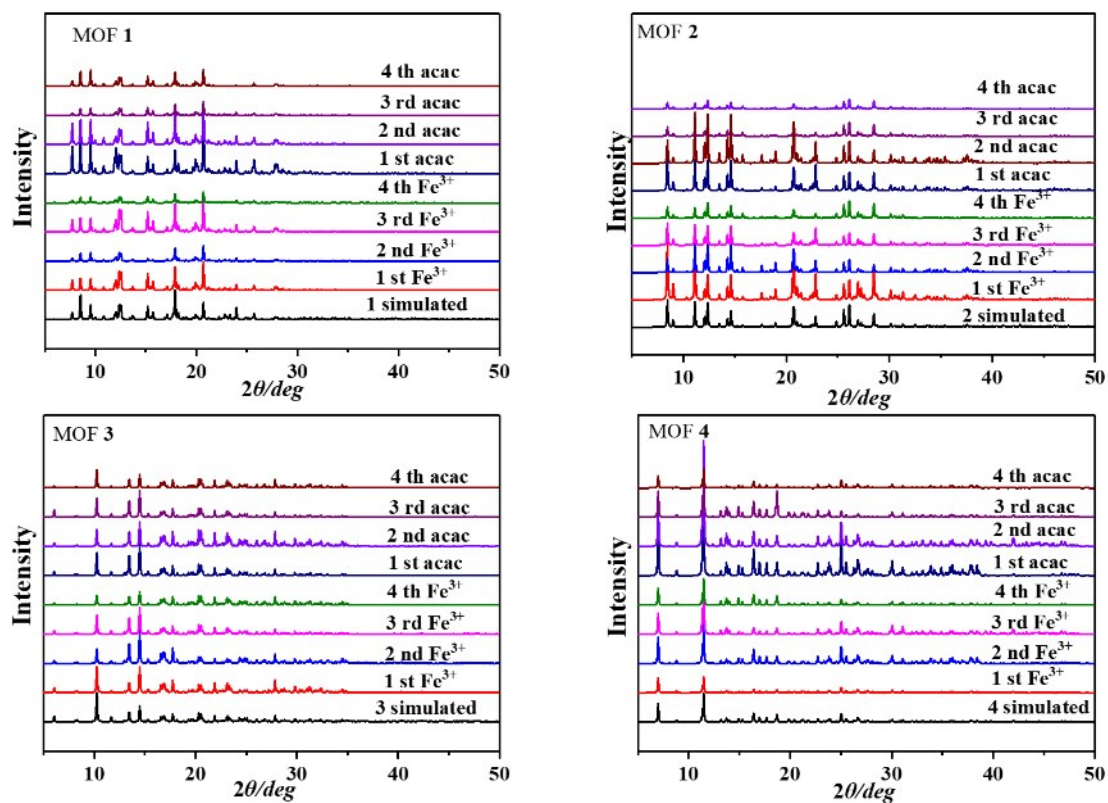


Fig. S23. PXRD patterns of MOFs 1-4 after 4 cycles of detecting  $\text{Fe}^{3+}$  or acac

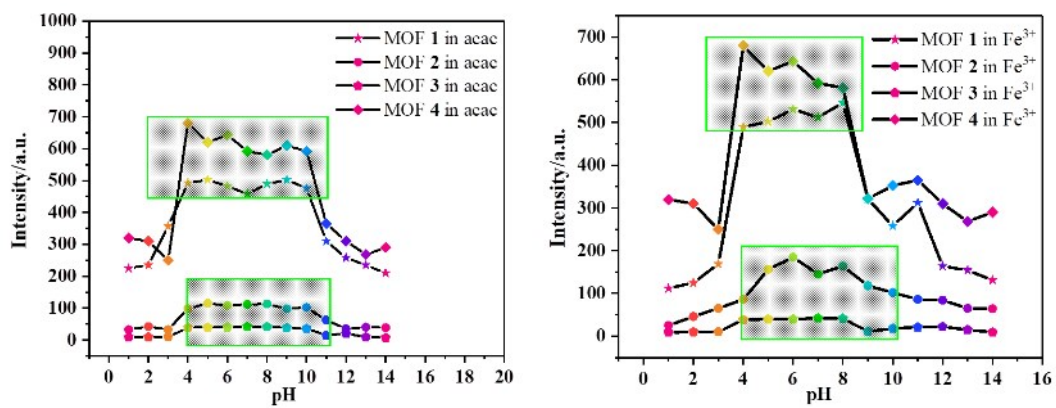
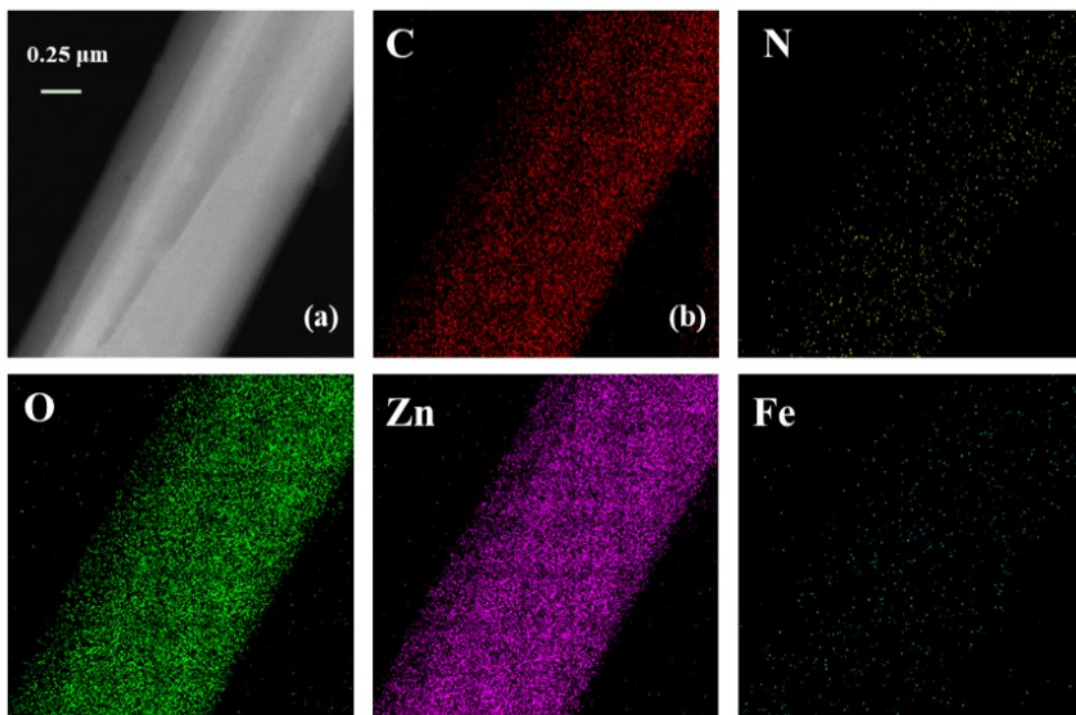
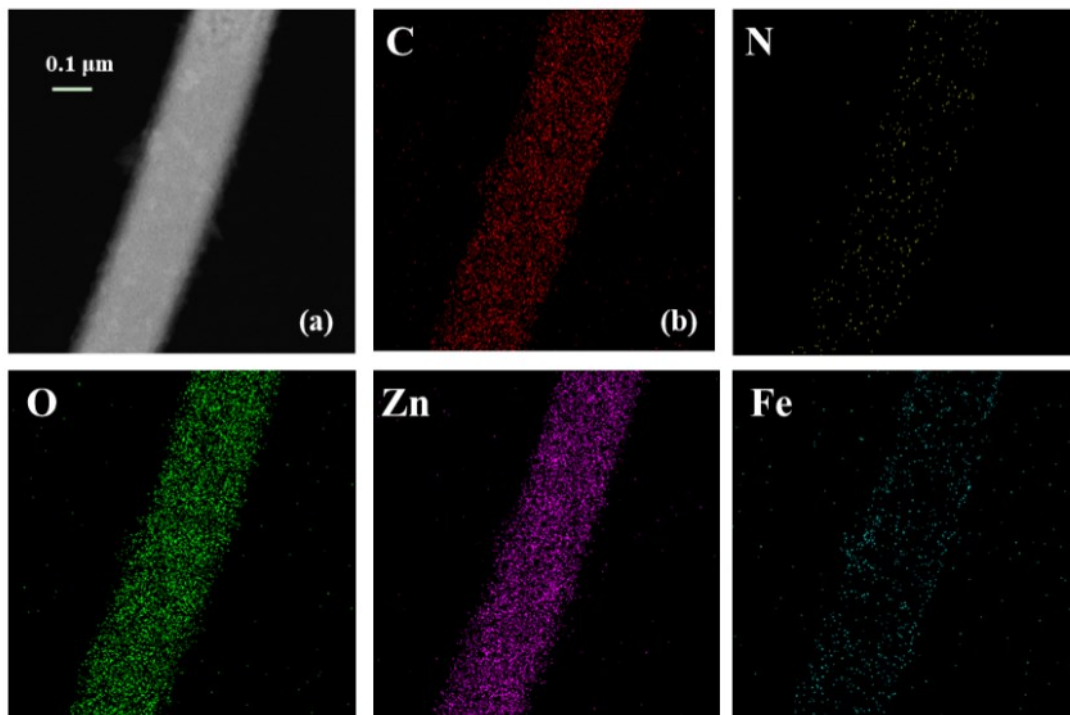


Fig. S24. (a) Effects of pH on the fluorescence maxima of MOFs 1-4 + acac and MOFs 1-4 + Fe<sup>3+</sup>.



**Fig. S25.** (a) TEM image of MOF 2, (b) TEM elemental mapping images of C, O, N, Zn and Fe in MOF 2 after detecting  $\text{Fe}^{3+}$  ions.



**Fig. S26.** (a) TEM image of MOF 3, (b) TEM elemental mapping images of C, O, N, Zn and Fe in MOF 3 after detecting  $\text{Fe}^{3+}$  ions.

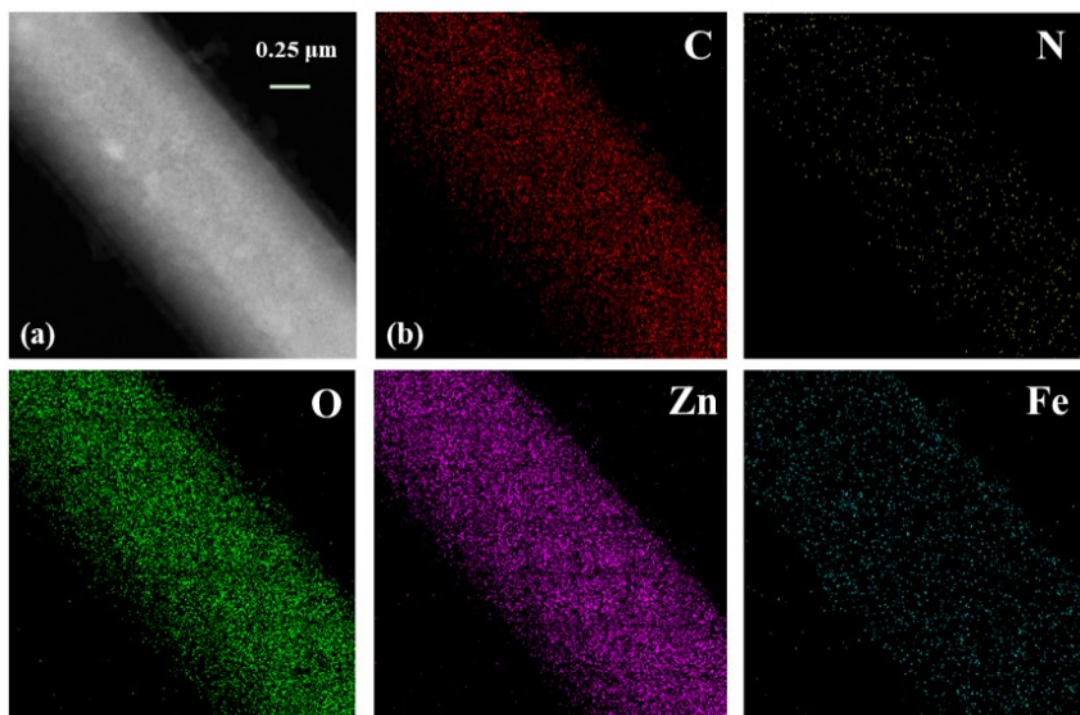


**Fig. S27.** (a) TEM image of MOF 3, (b) TEM elemental mapping images of C, O, N, Zn and Fe in MOF 4 after detecting  $\text{Fe}^{3+}$  ions.

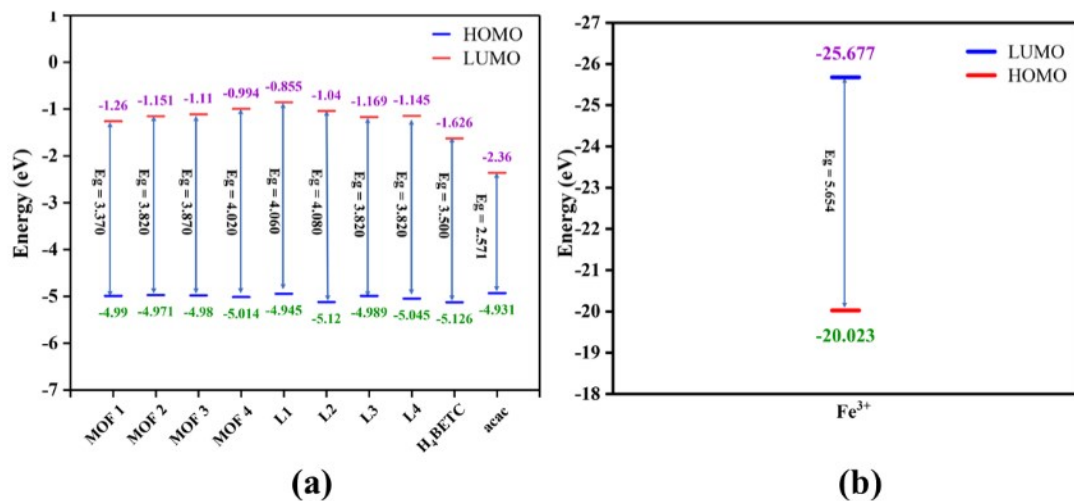


**Fig. S28.** (a) HOMO and LUMO energy levels for MOFs 1-4, L1-L4, H<sub>4</sub>BETC ligands and acac;

(b) HOMO and LUMO energy levels for Fe<sup>3+</sup>.

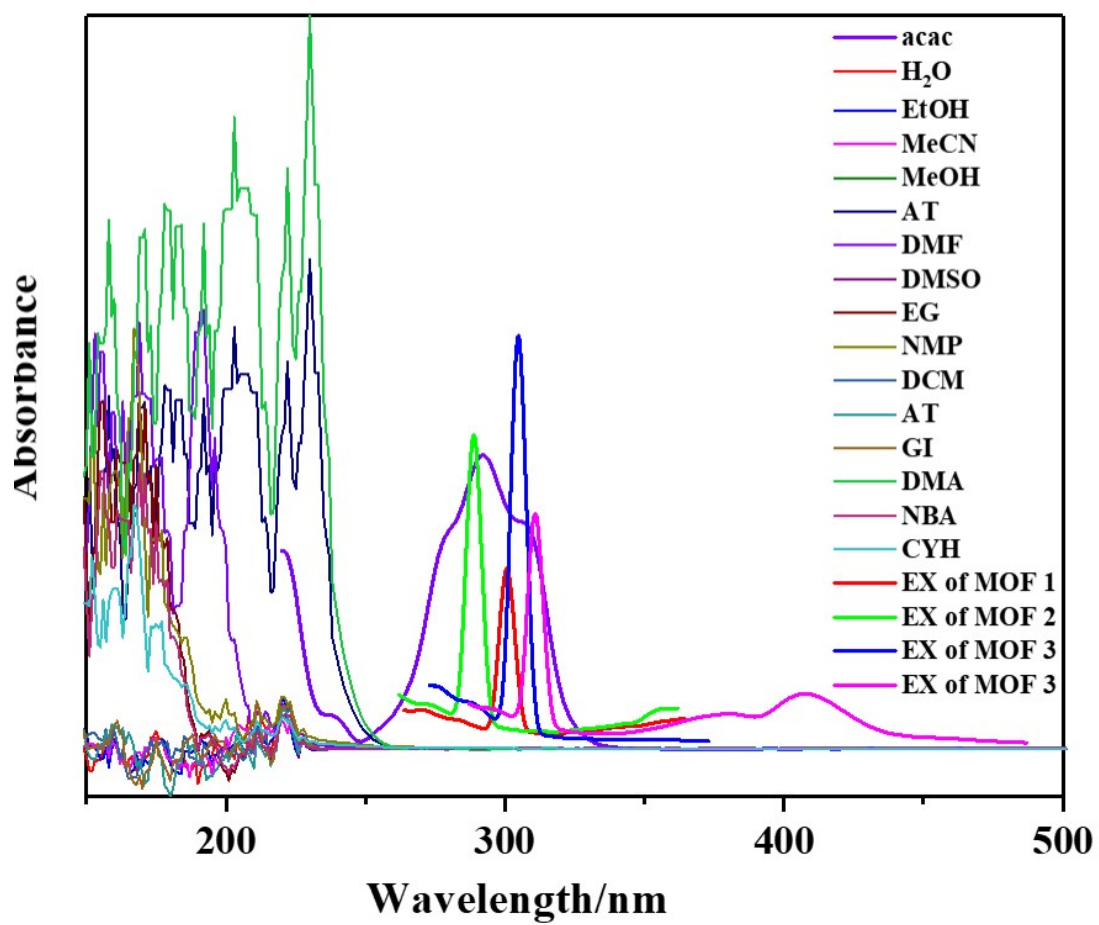


Fig. S29. Spectral overlap between the absorption spectra of acac ions and the excitation spectra of MOFs 1-4.

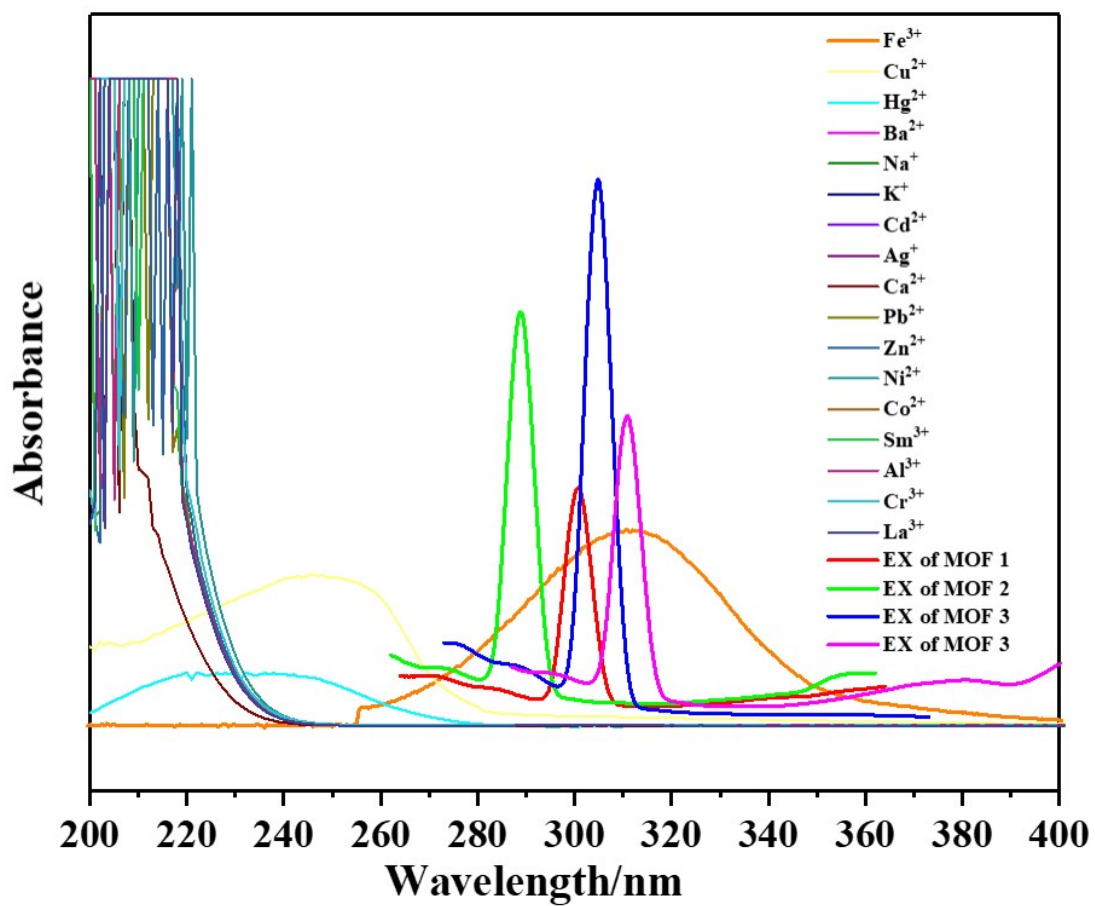


Fig. S30. Spectral overlap between the absorption spectra of Fe<sup>3+</sup> ions and the excitation spectra of MOFs 1-4.

### **Section 3. Supplementary Characterizations**

1. Crystal Structure of  $\{[\text{Zn}(\text{L}2)_{0.5}(\text{BTEC})_{0.5}] \cdot 1.5\text{H}_2\text{O}\}_n$  (**2**)
2. Crystal Structure of  $\{[\text{Zn}_2(\text{L}4)(\text{BTEC})] \cdot \text{H}_2\text{O}\}_n$  (**4**)

### Crystal Structure of $\{[\text{Zn}(\text{L2})_{0.5}(\text{BTEC})_{0.5}] \cdot 1.5\text{H}_2\text{O}\}_n$ (**2**)

The asymmetric unit of **2** comprises one independent Zn(II) ion, half a L2 ligand, half a BTEC<sup>4-</sup> anion and BTEC<sup>4-</sup> anion (**Fig. S31a**). Both Zn(II) ions are located on a distorted  $\{\text{ZnO}_2\text{N}_2\}$  tetrahedral geometry, defined by two monodentate carboxylate oxygen atoms (O1, O3A; symmetry code: A:  $1-x, 2-y, 2-z$ ) from BTEC<sup>4-</sup> anions, two nitrogen atoms (N1, N3B; symmetry code: B:  $x, 1+y, z$ ) from two different L2 ligands. The Zn–N/Zn–O bond lengths fall between 2.011(1) and 2.055(1) Å, 1.937(1) and 1.942(1) Å, respectively. The bond lengths around Zn(II) ions range from 97.6(6) to 123.4(6)°.

In MOF **2**, the BTEC<sup>4-</sup> ligand adopts a  $\mu_4$ -bridging fashion, in which each of the four carboxylate groups are in a  $(\kappa^1-\kappa^0)-(\kappa^1-\kappa^0)-(\kappa^1-\kappa^0)-(\kappa^1-\kappa^0)-\mu_4$  monodentate mode. As depicted as **Fig. S31b** right, the adjacent Zn(II) ions are connected by BTEC<sup>4-</sup> anions to form a 1D  $[\text{Zn}_4(\text{BTEC})]_n$  straight chain with a Zn(II)⋯Zn(II) distance of 8.843 Å. The  $(\kappa^1)-(\kappa^1)-(\kappa^1)-(\kappa^1)-\mu_4$  bridging L2 ligands adopt the *cis*-conformation to form a ladder chain  $[\text{Zn}_4(\text{L2})]_n$  (**Fig. S31b** left). Finally, these 1D straight and ladder chains are further connected by binuclear clusters to form a 2D network (**Fig. S31c, Fig. S7a**). To gain better insight into the network of **2**, the complicated 2D framework was simplified using ToposPro software<sup>40</sup>, the L2 ligands (blue balls), Zn(II) ions (cyan balls) and BTEC<sup>4-</sup> anions (red balls) all simplified to 4-connected nodes. Therefore, the 2D layer can be considered as the  $\{4^2 \cdot 8^4\} \{4^3 \cdot 6^2 \cdot 8\} \{4^4 \cdot 6^2\}_2$  topology network, also known as **4,4,4L10** (**Fig. S32d, Fig. S7b**).

### Crystal Structure of $\{[\text{Zn}_2(\text{L4})(\text{BTEC})] \cdot \text{H}_2\text{O}\}_n$ (**4**)

Structural analysis reveals that MOFs **4** crystallizes in the monoclinic *P* $\bar{1}$  space group. The asymmetric unit is composed of two Zn(II) ions, half L4 ligand, two half BTEC<sup>4-</sup> anions, as well as one free water molecule (**Fig. S32a**). The six-coordinated Zn1 is a distorted  $\{\text{ZnO}_5\text{N}\}$  octahedral geometry coordinated by five oxygen atoms (O1, O2, O3C, O6C, and O8C; symmetry code: C:  $1-x, 1-y, 1-z$ ) from two BTEC<sup>4-</sup> anions and one pyridyl nitrogen atoms (N1) from a L4 ligand. While the five-coordinated Zn2 resides in a  $\{\text{ZnO}_4\text{N}\}$  coordination environment surrounded by four oxygen atoms (O4, O5, O6 and O7A; symmetry code: A:  $1-x, -y, 1-z$ ) from two BTEC<sup>4-</sup> ligands and one imidazolyl nitrogen atoms (N3B; symmetry code: B:  $1-x, 1-y, 2-z$ ) from one L4 ligands, causing in a distorted square pyramidal coordination geometry. The range of

Zn–O/Zn–N bond distances and bond lengths around Zn(II) ions is basically the same as MOF **3**.

The BTEC<sup>4-</sup> anions exhibits two different  $\mu_6$ -bridging modes with carboxylate group in  $(\kappa^1-\kappa^1)-(\kappa^1-\kappa^1)-(\kappa^1-\kappa^1)-(\kappa^1-\kappa^1)-\mu_6$  complicated modes. the adjacent Zn1 and Zn2 ions are connected by carboxylate groups to form a [Zn<sub>2</sub>O<sub>5</sub>] binuclear secondary building unit (SUBs) with a Zn(II)··Zn(II) distance of 4.168 Å and further concatenate the 2D [(Zn<sub>10</sub>(BTEC)<sub>2</sub>]<sub>n</sub> network (**Fig. S32b**). Different from L3, the L4 ligands adopt a *cis*-conformation with  $(\kappa^1)-(\kappa^1)-(\kappa^1)-(\kappa^1)-\mu_4$  mode to connect adjacent Zn(II) ions into a “X” like shape unit [(Zn<sub>4</sub>(L3)]. On the basis of these connection mode, the 2D [(Zn<sub>10</sub>(BTEC)<sub>2</sub>]<sub>n</sub> network are interconnected through the L4 ligands to extend the 2D layers into a 3D framework (**Fig. S32c, Fig. S9a**). Topologically speaking, the BTEC<sup>4-</sup> anions can degenerate into two unequal 6-connected node (red sphere), the Zn1, Zn2 centers act as 4-connected nodes (cyan sphere) and L4 act as 4-connected nodes (blue sphere). This network can be simplified as a rare (4,4,4,6,6)-connected **4,4,4,6,6T3** topology framework with the Schläfli symbol of {4<sup>2</sup>·8<sup>4</sup>} {4<sup>4</sup>·6<sup>2</sup>}<sub>4</sub> {4<sup>6</sup>·6<sup>6</sup>·8<sup>3</sup>} {4<sup>8</sup>·6<sup>6</sup>·8}

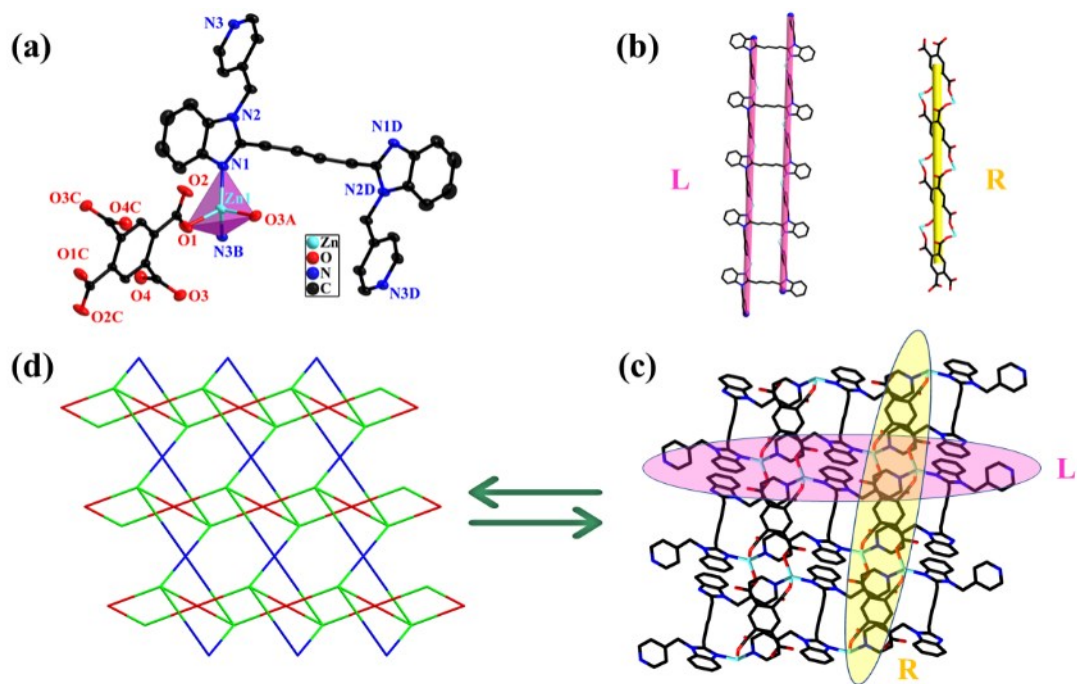


**Fig. S31.** (a) View of the coordination environment of Zn<sup>II</sup> in MOF 2 with the ellipsoids drawn at the 30% probability level (H atoms are omitted for clarity, symmetry code: symmetry code: A:  $1-x, 2-y, 2-z$ ; B:  $x, 1+y, z$ ; C =  $2-x, 2-y, 2-z$ ; D:  $-x, 1-y, 2-z$ ); (b) the ladder chain  $[Zn_4(L2)]_n$  was formed by L2 ligands and Zn<sup>II</sup> atoms, the BTEC<sup>4-</sup> anions create a 1D infinite  $Zn_4(BTEC)]_n$  chain by linking adjacent Zn<sup>II</sup> atoms in MOF 2; (c) in MOF 2, the two structures,  $[Zn_4(L2)]_n$  and  $Zn_4(BTEC)]_n$ , are cross-linked into 2D network structures in different directions; (d) a rare 2D structure with the **4,4,4L10** topology (cyan spheres: Zn<sup>II</sup> atoms; red spheres: BTEC<sup>4-</sup> anions; blue spheres: L2 ligands).

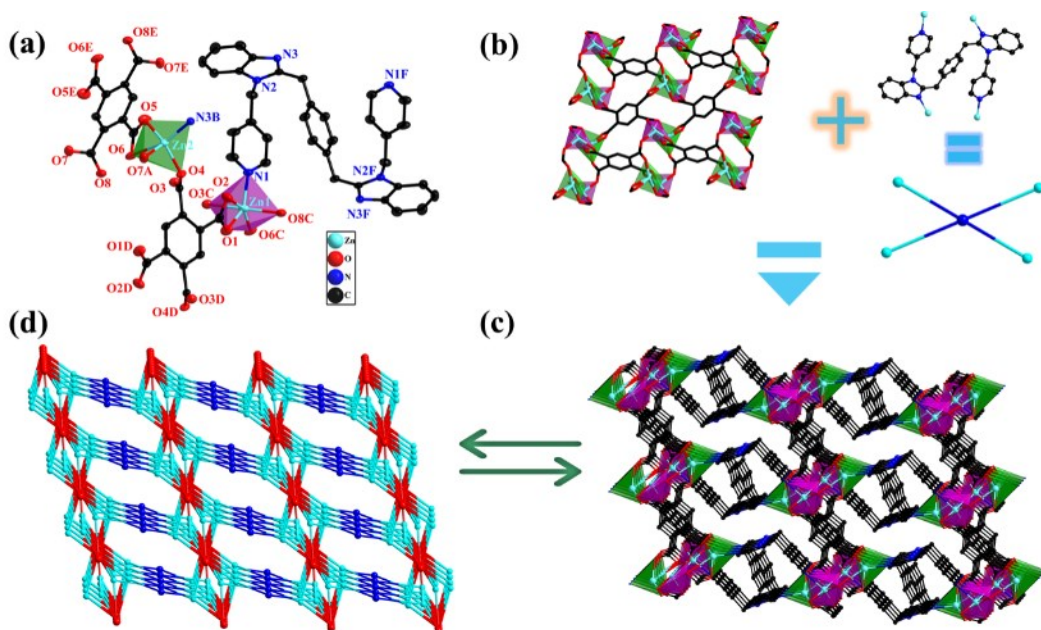


**Fig. S32.** (a) View of the coordination environment of Zn<sup>II</sup> in MOF 4 with the ellipsoids drawn at the 30% probability level (H atoms are omitted for clarity, symmetry code: A: 1-x, -y, 1-z; B: 1-x, 1-y, 2-z; C: 1-x, 1-y, 1-z; D: 2-x, 1-y, 1-z; E: -x, -y, 1-z; F: 1-x, 2-y, 2-z); (b) The 2D [(Zn<sub>10</sub>(BTEC)<sub>2</sub>)<sub>n</sub>] network network formed by Zn<sup>II</sup> and BTEC<sup>4-</sup> ligands in MOF 4 and one [Zn<sub>4</sub>(L4)] unit with the surrounding Zn<sup>II</sup> atoms in MOF 4; (c) a 3D layer structure formed by [[Zn<sub>4</sub>(L4)] units and [(Zn<sub>10</sub>(BTEC)<sub>2</sub>)<sub>n</sub>] network; (d) A rare (4,4,4,6,6)-connected 3D structure with the 4,4,4,6,6T3 topology in MOF 4 (cyan spheres: Zn<sup>II</sup> atoms; red spheres: BTEC<sup>4-</sup> anions; blue spheres: L4 ligands).